Doctoral Thesis

Study of MEMS Motion Sensors to Measure Multiple Physical Quantities Simultaneously

September 2023

Doctoral Program in Advanced Mechanical Engineering and Robotics

Graduate School of Science and Engineering

Ritsumeikan University

SIDDIQUE Kamran

Doctoral Thesis Reviewed

by Ritsumeikan University

Study of MEMS Motion Sensors to Measure Multiple Physical Quantities Simultaneously
（多種物理量が同時計測できる MEMS 運動センサーの研究）

September 2023

2023 年 9 月

Doctoral Program in Advanced Mechanical Engineering and Robotics

Graduate School of Science and Engineering

Ritsumeikan University

立命館大学大学院理工学研究科

機械システム専攻博士課程後期課程

SIDDIQUE　Kamran

シディーク　カムラン

Supervisor：Professor OGAMI Yoshifumi

研究指導教員：大上　芳文教授

Acknowledgements

I would like to express my deepest gratitude to my supervisor for his invaluable feedback and guidance throughout my PhD journey. His unwavering support and mentorship have been instrumental in shaping my research and academic growth. I am also thankful to my colleagues and lab mates who have assisted and accommodated me, despite the language barrier. Furthermore, I am grateful for the generous Monbukagakusho (MEXT) Government of Japan scholarship, without which this endeavour would not have been possible. This prestigious opportunity has allowed me to pursue my post-graduation studies in the captivating land of the rising sun.

I would like to express my deepest appreciation to my family and friends for their unwavering moral support throughout this journey. Their belief in me has been a constant source of inspiration, keeping my spirits high and motivation unwavering. I am also grateful for the countless cups of coffee that fuelled my early mornings and afternoons, without which this endeavour would not have been possible.

Lastly, I would like to dedicate this achievement to my father, whose unwavering inspiration and boundless motivation has been the driving forces behind my pursuit of this dream. This thesis is a testament to his profound influence and the enduring impact he has had on my academic and personal journey.

Table of Contents

List of Tables

List of Figures

Abstract

In this study, a new technique by which multiple physical quantities can be simultaneously measured with one motion sensor has been proposed by numerical simulations. The sensor is a modification of existing physical sensors such as a thermal motion sensor. Cross-axis sensitivity is an error in such devices, and lower values are generally targeted for the accurate performance of the device. In this study, however, errors in devices are utilized to simultaneously measure two or more physical quantities simultaneously using a single motion sensor. Three different cases are studied: 1) X-acceleration and Z-rotation; 2) X-acceleration and Z-amplitude of vibration; and 3) measuring acceleration and rotation in all three directions. The physics involved in measurement is similar to that of a conventional thermal accelerometer, hence the governing equations predicting the sensor response are based on the conservation of mass, momentum, and energy, and are solved by using the commercially available software ANSYS FLUENT. Obtained temperature responses are correlated with input physical quantities, and a graphical relationship (inverse function) is created between the peak temperature values and input physical quantities. Another novel approach known as 2D or 3D mapping is also proposed in which instead of using inverse functions, input physical quantities can be numerically and geometrically calculated from the output data, obtained by computational fluid dynamics (CFD) simulations using ANSYS FLUENT. A parametric study is also presented to find the optimum distance between the heater and sensors. The influence of changing gas medium on the temperature curves has also been examined and it has been concluded that CO_2 generates the maximum performance due to its higher density and lower viscosity. This thesis offers a novel approach to sensor technologies in unmanned aerial vehicles (UAVs) and similar devices, that will reduce the volume of sensors, the manufacturing and maintenance expenses through a decrease in the number of sensors required.

Chapter 1: Introduction

Sensor technology and development has been an important breakthrough in industrial science and engineering. Over the years, research has been conducted for the design and manufacturing of efficient, handy, and cost-effective sensors. The development of micro and nanotechnology has further enabled the miniaturization of these sensors while maintaining performance. Sensor applications have increased a lot over the years and multiple sensors are incorporated into engineering devices. One problem that has been pointed out recently is associated with the incorporation of multiple sensors into such engineering devices. For micro- and insect-scaled unmanned aerial vehicles (UAVs), installing multiple sensors to measure each physical quantity not only imposes higher manufacturing and repair costs but can also be time-consuming. Therefore, to solve this problem, in our study, we propose a novel idea which would allow the measurement of multiple physical quantities by employing a smaller number of sensors. This study will provide a new cost-effective and time-saving approach.

In micro- and insect-scaled UAVs, a range of sensors including GPS, ultrasonic sensors, and magnetic sensors are incorporated [1]. Among these sensors, accelerometers and gyroscopes play a vital role as they enable the UAV to determine its position by measuring acceleration and rotational speeds along all three axes, respectively [2]. In UAVs, there are various types of accelerometers, and thermal accelerometers offer specific benefits due to their lack of solid-proof mass for operation. These sensors are characterized by their compactness, lightweight design, ability to detect small accelerations, and lower initial costs [3].

In addition to UAVs, the rising prevalence of sensors in electronic devices like smartphones and the automotive industry, highlights the necessity to reduce the overall sensor count. Engine of a car alone has 15-30 sensors, while overall sensors in a car can reach up to 70. With the current shifting of technology towards C.A.S.E (Connected, Autonomous, Shared & Services, Electric) this number is expected to be increased. Therefore, ideas such as the one presented in this paper will not only inspire researchers and industrialists all around the world to investigate such matter but also provide a concept backed by empirical findings by which two physical quantities can be simultaneously measured by a single sensor.

The technique presented in this study does not involve creating a completely new device but modifying existing motion sensors, such as thermal accelerometers. A conventional accelerometer measures acceleration in all three directions. We have realized in our previous

studies [4], [5] that in addition to acceleration, change in temperature (ΔT) in a thermal accelerometer can also be correlated with other physical quantities, such as rotational speed, and amplitude of vibration. This is accomplished by considering the cross-axis sensitivity, which is the sensitivity observed in the plane perpendicular to the measuring direction relative to the measuring direction. Ogami [6] suggested that cross-axis sensitivity should not be removed but rather exploited. In this way, if multiple motion types are applied on a single axis, with sensitivities observed in other axes, the input physical quantities will have a relationship with the output sensitivities. In this study, a thermal motion sensor is considered; using cross-axis sensitivity, we have presented a technique by which we can measure acceleration and rotational speed/amplitude of vibration, simultaneously.

In addition to introducing a novel approach to achieve our objective of measuring multiple physical quantities, we have also presented a parametric study to enhance the sensitivity and resolution of the motion sensor. For that, we have considered the effect of the change of gas medium of the device and the distance between the heater and temperature sensors, as these two factors greatly influence the overall performance of the device.

In this study, we have utilized a FEM simulator ANSYS FLUENT 18.2 and provided computational results. While the results using Computational Fluid Dynamics (CFD) are reliable and have been employed by researchers over the year for various studies, verification of the results with an experimental model is necessary. This study does not provide such validation, hence, it's one of the limitations of this study. To thoroughly understand the research work, it is important to understand some terminologies, which have been described in detail along with the essential literature references in **Chapter 2**. The extended methodology and justifications for the choice of the computational model and simulation conditions are written in detail in **Chapter 3**. We have considered two different computational models, hence two different meshes to accomplish our goals. As described in **Chapter 4**, three cases are considered. For the first two cases, we utilized the design of a dual-axis motion sensor, while accomplishing the result of measuring acceleration and rotation in all three directions required a triple-axis motion sensor (case 3). The result data presented in section **4.1** is published in [4], while the result in section **4.3** is published in [5]. Sections **4.2** and **4.4** are unpublished works which are being presented in this thesis.

Chapter 2: Literature Review

2.1 CFD Technology

Computational Fluid Dynamics (CFD) is a branch of Fluid Dynamics that utilizes numerical analysis and data structures to solve fluid flow problems by solving the Navier-Stokes equation. CFD simulates fluid flow by iteratively reducing the error between the approximate solution and the partial differential equation solution through numerical methods such as the finite element method (FEM), finite difference method (FDM), and finite volume method (FVM) [7].

Several software codes to solve fluid flow problems are commercially available: ACE+ [8], CFX [9], FLOW-3D [10], and FLUENT [11]. Expect for FLOW-3D, all these software uses the finite volume method (FVM) to solve the governing equations of fluid flow and heat transfer. Flow-3D is based on a combination of finite difference and finite volume perspectives, and it uses a control volume approach to solve the conservation equations.

To run a CFD analysis, it is important to first understand and analyse the problem at hand and what the end goal is expected, this includes deciding on the geometry type and initial and boundary conditions. Next, a computer-generated design (CAD) model is generated using either CAD software or integrated features within ANSYS Workbench. Next, a mesh or a grid of the CAD model needs to be generated and there are two tools accessible for the purpose of grid generation: ANSYS DesignSpace in combination with AI*Environment and ICEMCFD. In contrast to other tools, both ANSYS Workbench and ICEM CFD cannot be controlled via a scripting language; ANSYS Workbench however can handle parameterized geometries. ICEM CFD has only basic modeling capabilities but supports a wide range of mesh operations and mesh types [12]. ANSYS Meshing tool can be utilized to create either a structured mesh (quadrilateral in 2D and hexahedron, prism/wedge in 3D) or an unstructured ((triangle in 2D and tetrahedron, pyramid in 3D), depending on the problem at hand. Sometimes, hybrid meshes or non-conformal meshes are also generated. A non-conformal mesh is formed when there is partial or zero matchings of nodes at the interface.

After an appropriate mesh is formed, FLUENT is used for the simulation process, the solving process, and post-processing. All the Graphical User Interface (GUI) commands are scripted by the program. However, the existing codes of FLUENT can be modified by User-Defined Functions (UDFs), which are functions that the user can program (write a code) which can be dynamically loaded with the FLUENT solver to improve the standard function of the code [13].

CFD is capable of handling complex geometries and reconstructing real-life conditions to generate high-quality results.

CFD has numerous advantages and has been employed in literature for achieving several tasks. Some of the applications of CFD include designing and analysing heating, ventilation, and air conditioning (HVAC) systems [14], in food processing industries including drying, sterilization, refrigeration, and mixing [15] and aerodynamics design of aircraft [16] amongst numerous others. Practically, any phenomenon in nature or a system in which a fluid (gas or liquid) is flowing inside or over an object can be studied, analysed, and optimized using CFD technology.

Along with the benefits of using CFD, there are of course some limitations as well that need to be taken into account, some of which are listed below.

1. There are limitations to how physical phenomena can be modeled into a geometry.
2. Creating a mesh for complex structures is difficult.
3. Not all boundary conditions in nature can be replicated.
4. For complex systems, computation time is high.

Therefore, keeping this in view, it is important to verify the results of CFD with theoretical or experimental models. Currently, however, CFD has been integrated with state-of-art technologies such as artificial intelligence, machine learning, and virtual reality which widens the applications and possibility of achieving accuracy with CFD.

2.2 Sensor Technology in Unmanned Aerial Vehicles

Unmanned Aerial Vehicles (UAVs) offer a cost-effective and time-saving way to perform various functions, providing a level of safety and convenience compared to traditional methods. They have a wide range of uses and can be crucial for multiple applications and industries. They can be useful for search and rescue operations [17], including disaster relief and emergency response. They can be used to deliver packages and goods to remote areas or places where road access is impossible. In addition, UAVs can be used for inspecting infrastructure such as buildings and bridges and high-quality images for taking the right decision through the monitoring approach [18] as well as for monitoring landslides [19]. Applications of UAVs in smart farming have also been growing rapidly. Praveen [20] described a thorough study of UAV applications in smart farming including the requirement and challenges. Recently, Amazon has introduced Amazon Prime Air which will deliver packages to people's doorstep using a drone [21]. Once an

order is placed by the customer, a drone carrying the package will fly to the customer's backyard, hover at a safe height, release the package, and finally fly back again. These are all very exciting and useful prospects that UAV technology will bring about as it grows further.

In a UAV system, various sensor and communication modules are integrated using computing platforms, as represented in Figure 1. Computing platforms are hardware processing units that can connect and act as a medium for processing data from various sensors and communication modules [22]. A UAV senses and perceives its surrounding by using several sensor modules, depending on the application and use of the UAV. Moreover, choosing a well-suited communication module for the specific application is essential, considering its characteristics. Wireless Fidelity (Wi-Fi) modules are well-known communication modules and are more commonly used to transfer information in UAVs.

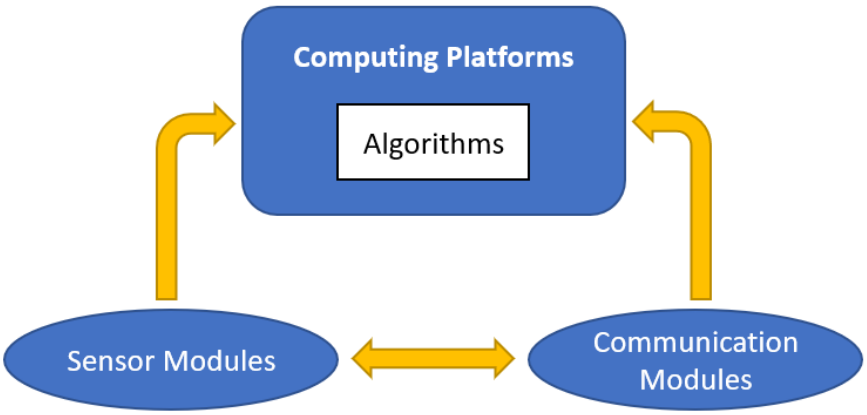

Figure 1- A UAV system

To enable the efficient and accurate functioning of UAVs, development in sensor technology is crucial along with the design and manufacturing technologies of UAVs. Linga [23] provided a description of the different types of sensors used in autonomous systems and a parametric comparison of frequency, power consumption, dimensions, and weight. Emad [24] presented a survey of open-source platform elements that are available including hardware, software, and simulation drone platforms. In a UAV, several sensors are installed, and each sensor type has specific functions. Table 1 presents a list of various sensor types along with their corresponding examples, and references to background studies. In this paper, however, the focus is on the Inertial Measurement Units (IMUs) i.e., accelerometers and gyroscopes that measure the position and orientation of UAVs.

Table 1- Classification and literature work of different sensor modules used in UAVs.

Category	Sensors	Relevant Literature
Vision-based sensors	RGB cameras, thermal cameras	[25]–[27]
Position-based sensors	GPS, accelerometers, gyroscopes, magnetometers	[28], [29]
Proximity sensors	Ultrasonic sensors	[30]
Radar-based sensors	mmWave frequency modulated continuous wave (FMCW) Radar	[31]
Wireless system sensors	Radio-Frequency Identification (RFID) Sensor and Ultra-Wideband (UWB) Sensor	[32], [33]

UAV states are generally estimated by fusing data from accelerometers, gyroscopes, and global navigation satellite systems (GNSS) to determine their pitch, yaw, and roll, as shown in Figure 2. Common types of MEMS gyroscopes used in UAVs include ring laser, fiber optic, MEMS vibrating structure, and Coriolis vibratory types. One major problem that occurs in these devices is the effect of environmental thermal fluctuations. The temperature compensations method had been presented by several researchers by changing the gyroscope structure to decrease the frequency variation under different temperatures [34], [35]. However, this limitation of MEMS gyroscopes remains a challenge. This study proposes a novel concept, which involves the measurement of rotational speeds in addition to acceleration, achieved by modifying a conventional thermal accelerometer that can measure only acceleration. To understand how this is achieved, it is important to understand the different types of MEMS accelerometers commonly used, which are described in detail in the next section.

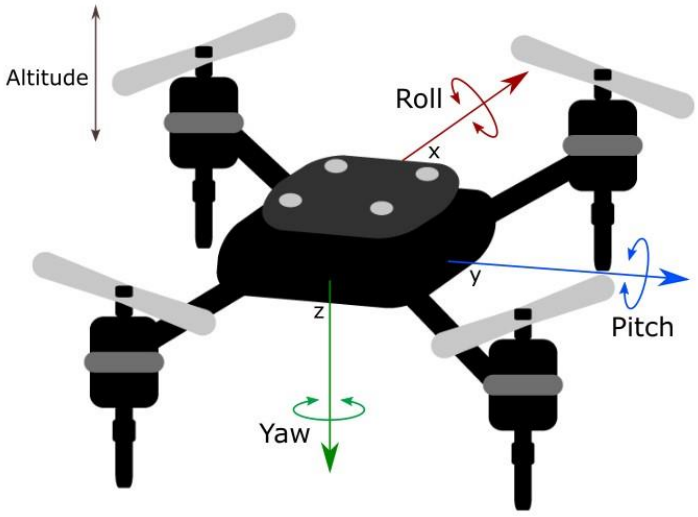

Figure 2- Drone's pitch, roll, and yaw.

2.3 MEMS Accelerometers

The significance of sensor technology in our society is undeniable. These are utilized in ensuring the proper operation of complex electronic structures and extracting valuable information from our environment [36]. Microelectromechanical system (MEMS) based sensor-actuator applications continue to grow in various industries due to their improved sensitivity, accuracy, and reliability of operations along with low power consumption [37]. The use of MEMS sensors for vehicular sensing has been gradually increasing [38]. MEMS accelerometers have substantially been utilized in UAVs owing to their compactness, lightweight, low power, and high sensitivity. Almost all sensing mechanisms (i.e., capacitive, piezoresistive, piezoelectric, thermal, optical, electromagnetic, tunneling) have been employed in various accelerometer designs, however, capacitive, piezoresistive, piezoelectric, and thermal accelerometers are among UAVs' commonly used MEMS accelerometer types.

Capacitive sensing has been one of the most commonly used sensing principles. An example of such a sensing device is demonstrated in Figure 3 which is adapted from [39]. In this type of accelerometer, as the proof mass is displaced by the acceleration, capacitance is sensed between the rotor and stator electrodes. The varying capacitors are connected to a differential capacitive bridge and the output signal is sensed by using a voltage amplifier. Simple structure and low-temperature sensitivity are the characteristics of capacitive-type accelerometers.

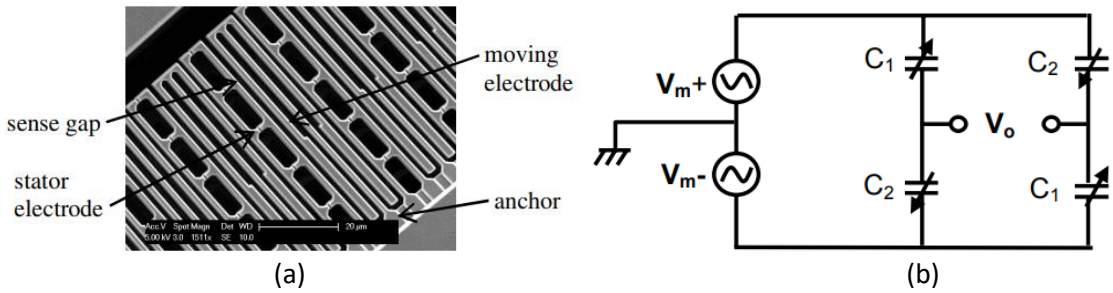

Figure 3- (a) A capacitive type accelerometer (b) the differential capacitive bridge model (adapted from [39]*).*

A piezoresistive accelerometer produces resistance changes in piezoresistive materials to convert mechanical strain to a DC output voltage. These devices provide extremely localized acceleration-induced stress sensing with low noise outputs and have been the subject of academic as well as commercial research for quite a few years [40]. The development of bulk micromachining and wafer bonding techniques saw a rise in piezoresistive accelerometer development toward low g applications [41]. The main advantages of piezoresistive accelerometers are the simplicity of their structures and the fabrication process used to manufacture them. Additionally, the readout circuitry is crucial due to the low output-impedance direct current (dc) voltage generated by the Wheatstone bridge. In 1995, Yuebin [42] manufactured a high g-force cantilevered type piezoresistive accelerometer that could sustain loads of up to 100,000 g. Lishuang [43] presented the design and optimization of a high-g piezoresistive accelerometer that could work normally under 200,000 g overloads. This shows that such types of sensors are suitable for working under heavy overload.

A piezoelectric accelerometer is an accelerometer that employs the piezoelectric effect of certain materials to measure dynamic changes in mechanical variables (e.g., acceleration, vibration, and mechanical shock). It consists of a mass attached to a piezoelectric crystal which is mounted on a case. When the accelerometer body is subjected to vibration, the mass of the crystal remains undisturbed in space due to inertia. They have a wide dynamic range, low output noise, and a wide frequency range [44]. In piezoelectric types, a strain of the piezoelectric film is converted into output voltage [45]. It has the advantages of high conversion efficiency and easy implementation [46], [47].

Stephan [48] did a performance analysis of different accelerometer types by considering data sheets of 118 accelerometers from 27 different manufacturers. It was found that piezoelectric accelerometers show the highest measurement range which can be more than 10,000 g. Thermal accelerometers, however, show outstanding shock limits of 50,000 g by low

measurement ranges of 5 g. Jiang [49] did an extensive overview of piezoelectric accelerometers and mentioned how these are effective for high-temperature applications such as aerospace, aircraft, automotive and energy industries. Thermal accelerometers, however, do not have a solid-proof mass, hence, the fabrication is simpler, integration of the sensor with the signal conditioning circuit is easier, and results in improved device durability and measurement consistency [50].

Accelerometers have diverse applications in the automotive, consumer electronics, and biomedical industries. Conventional accelerometers convert accelerations into electrical signals using several mechanisms, including piezoresistivity, piezoelectricity, and capacitive type. However, the use of a solid-proof mass in such devices imposes mechanical limitations on the amount of shock and the sensing range they can undergo. In contrast, the convective nature of a thermal accelerometer with no moving parts can increase the sensing range of such a device. The description of thermal-based accelerometers is written in detail in the next section.

2.4 Thermal Accelerometers (Thermal Motion Sensors) Theory

Thermal-based accelerometers offer several advantages over conventional proof-mass accelerometers. They exhibit no measurable resonance, delivering immunity to vibration; no temperature hysteresis, and excellent zero-g offset stability with the added shock resistance, hence increasing their reliability [51]. This enhances the sensing range of the device without failure or vibrational limitations. The concept of a thermal accelerometer is based on free-convection heat transfer using a working fluid (gas or liquid) as the working media in a sealed chamber [52]. A heating source generates a consistent temperature profile that is altered by applied acceleration; thus, this difference in temperature ΔT is related to the change in acceleration, as shown in Figure 4. In this figure, the thermal sensor consists of a single heating source that heats the surrounding gas, creating a symmetrical temperature profile (solid line in (right)). When no acceleration is applied, the equally spaced sensors placed on the sides of the heater detect the same temperature. However, when acceleration is applied, the difference in temperature ΔT is modified, creating an asymmetrical temperature profile around the sensor (dashed line in (right)). Figure 5 depicts a clearer image of the concept in terms of the temperature contours and a side view of a cylindrical cavity with two heating sources. The red part denotes the highest temperature at the heating sources, and that around the boundaries (dark blue) is at room temperature (300 K). When no acceleration is applied, the thermal bubble is consistent around the heating sources. However, when acceleration is applied, the thermal

bubble shifts in the direction of the applied acceleration. In this way, the pair of temperature sensors, placed equidistant from the heater, as shown in Figure 4, detect a difference in temperature, which is correlated with the change in acceleration.

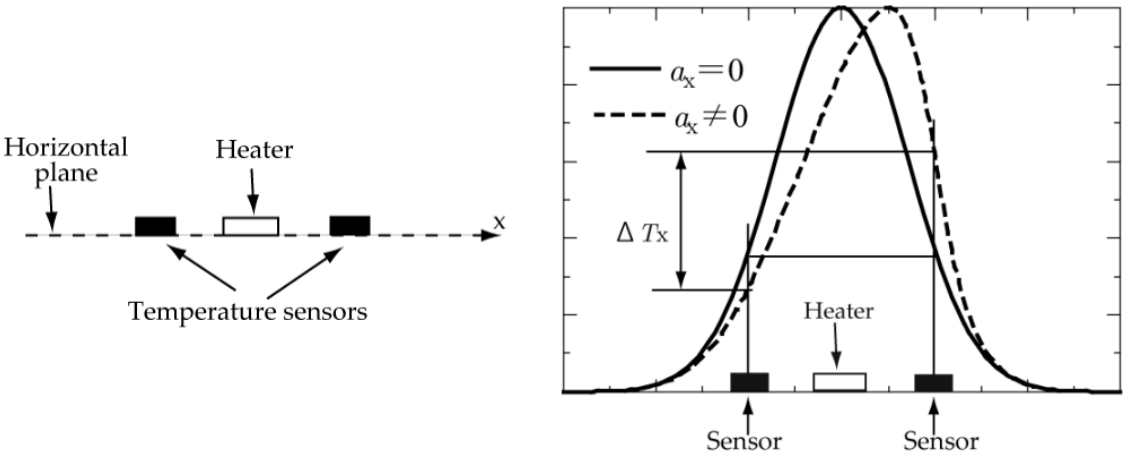

Figure 4- Heater and temperature sensors (left); temperature profile with and without acceleration (right) (adapted from [6]*).*

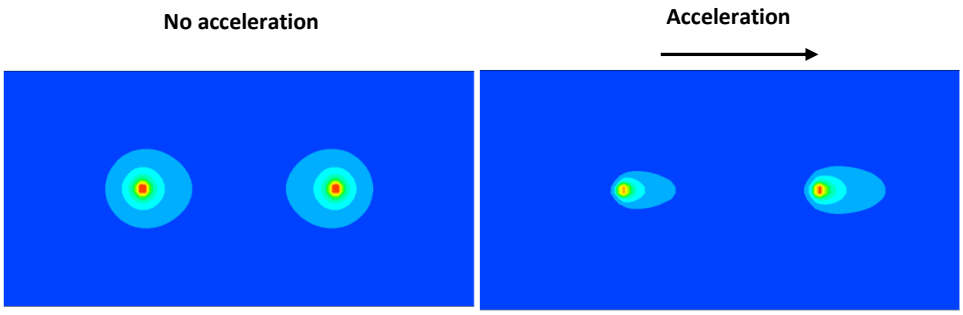

Figure 5- Temperature profile without acceleration (left) and with applied acceleration (right).

This can also be viewed in terms of isotherms from the above figure. As shown in Figure 6, sets of isotherms are created around the heating source, where isotherms near the heater have higher temperature values. Without the application of any motion, a consistent temperature profile is obtained as shown in Figure 6(left). However, when acceleration was applied in the right direction, the sets of isotherms shifted to the right Figure 6(right).

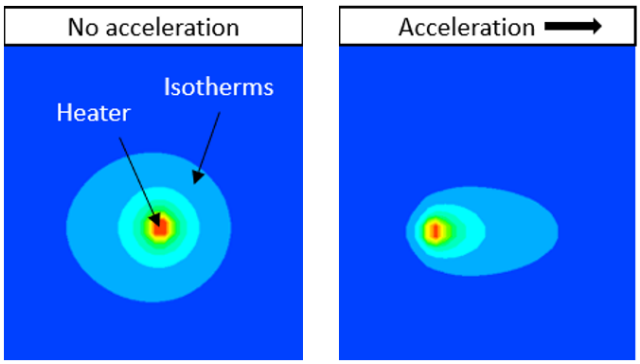

Figure 6- Change in isotherms with no acceleration (left) and acceleration applied to the right side (right).

Different numerical and experimental studies have been conducted to optimize multiple-axis thermal accelerometers. Novel triple-axis thermal accelerometers were introduced by [53] and improved by [54]. However, their sensitivities were still insufficient and required further improvement. Mukherjee [55] modified the cavity structure of the device to achieve better sensitivity. Jiang [56] showed that increasing heater power enhanced the sensitivities along the X-, Y-, and Z-axes. Wang [57] achieved improved sensitivity and a wider ambient temperature measurement range in a recent study. This design can detect precisely in environments with varying temperatures. In this study, we aimed to select the parameters that resulted in high sensitivity and resolution, as reported in studies.

For a dual-axis thermal accelerometer, two sets of temperature sensors are needed around two axes, on the other hand, three sets of temperature sensors to detect temperature around X, Y, and Z-axes are needed for a triple-axis thermal accelerometer. To reduce the installation and maintenance costs, Ogami's concept [6], which uses cross-axis sensitivity (CAS), can be used. Due to CAS, when a motion is applied to a single axis, the correlating temperature change is also observed at the other two perpendicular axes. According to Farahani [58], CAS is a good measure of sensor performance in response to external factors. Therefore, for high-accuracy applications, a lower CAS is expected. In this study, using fluid flow and thermodynamic principles and leveraging CAS, we were able to measure multiple physical quantities simultaneously. The concept of CAS is described in detail in the next section.

2.5 Cross-axis Sensitivity

Cross-axis sensitivity (CAS) is the maximum sensitivity in the plane perpendicular to the measuring direction relative to the sensitivity in the measuring direction. It is calculated as the geometric sum of the sensitivities in two perpendicular directions (Sx and Sy) in this plane. This

is explained in Figure 7. A ball inside a box is being accelerated in the positive x-direction. With no effect of CAS, acceleration is detected by the X-sensor and there is no detection at the Y-sensor. This should be the ideal condition for a sensor. However, even when there is motion in the X-direction only, the Y-sensor also detects some value, which is an error in such devices known as CAS. It is commonly observed in accelerometers and gyroscopes.

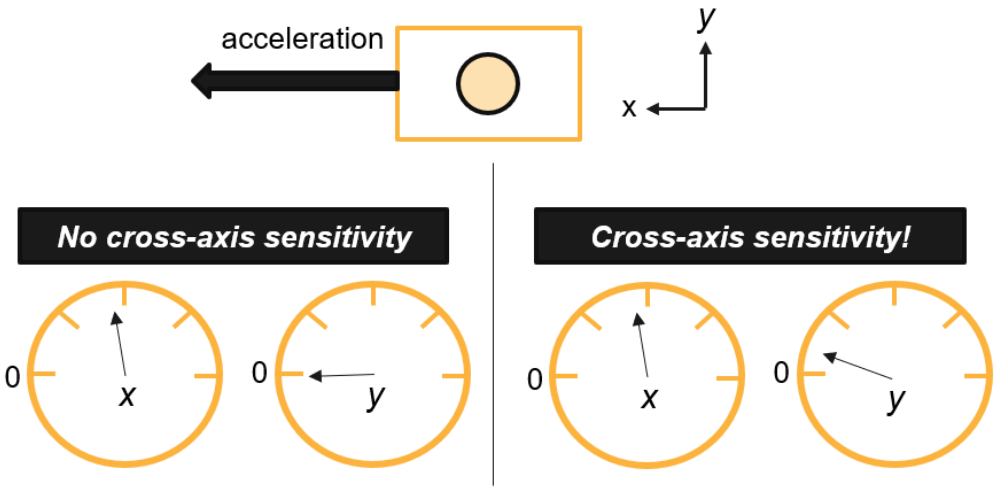

Figure 7- Description of X and Y sensor response of a body accelerating in the x-direction with and without cross-axis sensitivity.

To have a reliable MEMS accelerometer device, the performance requirements for consumer devices include multi-axis operation, low noise floor, low cross-axis sensitivity, low nonlinearity, and low power consumption. Therefore, in the literature, several research has been conducted to study such errors in devices and methods to reduce them. Zine [59] presented a mathematical model in which mechanical sensitivity is developed as a function of the measurement error of a vibration sensor. Yu [60] developed a compact accelerometer, which integrates three spring-proof mass systems into a single structure to sense triaxial motion. Cross-axis sensitivities of the x-axis and y-axis in-plane accelerometers were observed to be 0.03% and 0.21%, respectively.

Cross-axis sensitivity can be significantly reduced in single-axis accelerometers [61], however, it is difficult to target very low cross-axis sensitivities in double-axis or triple-axis accelerometers. This is because the geometrical structure for the tri-axial accelerometer is designed in such a way that the structure is sensitive to all three axes [62]. Shan [63] presented a micro-grating accelerometer with a double-layer cantilever beam. Theoretical results showed

that the symmetrical design of the double-layer cantilever beams structure could effectively reduce the cross-axis sensitivity. Hadi [64] on the other hand, introduced a new technique to eliminate the cross-axis sensitivity in a 3-axis MEMS capacitive accelerometer based on the orientation and location of the electrodes.

Shan [63] demonstrated the relationship between the output of acceleration and acceleration along the sensitive axis. Ideally, the accelerometer can accurately detect the acceleration along the sensitive axis, as shown by the blue line in Figure 8. However, if the accelerometer has cross-axis sensitivity, the output of the accelerometer will be affected by the acceleration along the insensitive axis and become inaccurate.

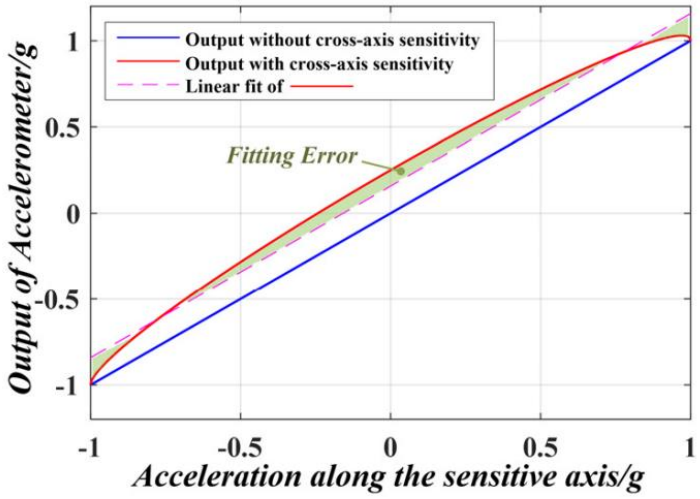

Figure 8- Output of accelerometer with or without cross-axis sensitivity (adapted from [63]).

In summary, this research study leverages the extensively researched error found in the literature for thermal accelerometers to be effectively used as an advantage to measure multiple physical quantities simultaneously.

2.6 Sensitivity, Frequency Bandwidth, and Resolution of Thermal Motion Sensors

The sensitivity and frequency bandwidth of any sensor device plays important roles in defining its performance. Sensitivity is the minimum input of the physical parameters that creates a detectable output change. Frequency bandwidth is a measure of how quickly the sensor can respond to changes in input physical parameters. Resolution is defined as the smallest change in a quantity being measured that cause a perceptible change in the corresponding indication in measured quantity. Over the years, various analytical studies and computational simulations have been conducted to predict the sensitivity and frequency bandwidth of

Microelectromechanical Systems (MEMS) thermal accelerometers. The thermal accelerometer was first reported by Albert [65] in 1997. Dimitris [66] developed a conductive thermal accelerometer comprising a polysilicon heater and two thermopiles. This device uses electrical energy as a parameter related to thermal energy. However, the literature has mentioned that obtaining the temperature profile using temperature sensors and relating it to the input thermal energy generates better results. Brahim [67] developed a 3D model for FEM simulations using a derived analytical model to study the conductive behaviour of MEMS thermal accelerometers.

Researchers have developed theoretical, computational, and experimental models for improving the performance of thermal accelerometers. It has been observed that a high heating power and a large device size leads to an increase in sensitivity [68]. However, an increase in the pressure of the air medium results in a decrease in the frequency bandwidth. Additionally, gas media with high densities and low viscosities appear to result in better sensitivity [69]. Leung [65], [70] demonstrated that the sensitivity of a thermal accelerometer is linearly proportional to the Grashof number (Gr):

$$Gr = \frac{g\rho^2\beta L^3\Delta T}{\mu^2}$$

$$Pr = \frac{\mu}{\alpha}$$

where, ρ, β, L, ΔT, μ, and α are the applied acceleration, gas density, coefficient of volumetric expansion, characteristic size (generally denotes the cavity size), the temperature difference between the heater and the boundary of the sensor, kinematic viscosity, and thermal diffusivity, respectively. These parameters can be used to predict the device's performance. From the above equations, it can be observed that the sensitivity of the device can be significantly increased by using a high-density and low-viscosity fluid. The properties of some fluids and their calculated Gr and Prandtl (Pr) numbers are listed in Table 2 and Table 3, respectively. These parameters can be modified and optimized to increase the sensitivity of a thermal accelerometer.

Table 2- Gas medium properties at 50 °C (adapted from [71]*).*

	Density (kg/m³)	**Specific Heat (kJ/kg·K)**	**Kinematic Viscosity (×10−6) (m² /s)**	**Thermal Diffusivity (×10−4) (m² /s)**	**Thermal Conductivity (W/m·K)**
Air	1.092	1.007	19.6	0.248	0.02735
N_2	1.0564	1.042	17.74	0.249	0.02746
CO_2	1.6597	0.8666	9.71	0.129	0.01858

Table 3- Calculated Gr and Pr numbers.

	Air	**N_2**	**CO_2**
Gr	7.44×10^{-3}	8.07×10^{-3}	4.24×10^{-2}
Pr	7.16×10^{-4}	6.46×10^{-4}	5.22×10^{-4}

As seen from Table 2 and Table 3, CO_2 has the highest density and lowest kinematic viscosity, as a result, it has the highest Grashof number. In comparison, the air has a lower density to kinematic viscosity ratio and hence a lower Gr value in comparison to CO_2. High viscosity yields high resistance to gas flow and in return lower sensitivity.

2.7 Scope of this Study

One problem that has been pointed out recently is associated with the incorporation of multiple sensors into engineering devices. For micro- and insect-scaled unmanned aerial vehicles (UAVs), installing multiple sensors to measure each physical quantity not only imposes higher manufacturing and repair costs but can also be time-consuming. Therefore, to solve this problem, in our study, we propose the novel idea that in addition to acceleration, ΔT can also be correlated with other physical quantities, such as rotational speed, amplitude, and frequency of vibration. This technique does not involve creating a completely new device but modifying existing motion sensors, such as thermal accelerometers. This is accomplished by considering the cross-axis sensitivity, which is the sensitivity observed in the plane perpendicular to the measuring direction relative to the measuring direction. Ogami [6] suggested that cross-axis sensitivity should not be removed but rather exploited. In this way, if multiple motion types are applied on a single axis, with sensitivities observed in other axes, the input physical quantities will have a relationship with the output sensitivities. It has been observed that other physical quantities such as rotation and vibration can also be measured when applied along with a perpendicular acceleration. In this study, a thermal motion sensor is considered; using cross-axis sensitivity, we

can measure the acceleration and rotational speed, and acceleration and amplitude (of vibration) simultaneously.

In addition to providing the concept of this novel methodology, a parametric study is also conducted in which two of the important parameters i.e., the distance between heater and sensors, and gas medium are altered, and results are obtained in comparison to the sensitivities and resolutions of the motion sensor. This ensures developing a sensor that has a high sensitivity and performance.

The inverse functions obtained can then be installed in the computing unit of a real thermal motion sensor so that the sensor can calculate the values of the input physical quantities from the output values (measured temperature values). We believe, this concept if commercialized, can provide an innovative and cost-effect solution to, not only UAVs but several industries and products.

Chapter 3: Methodology

In this study, ANSYS FLUENT 18.2 was employed to perform computational analyses. A parametric study can be conducted because the software accommodates changing flow (initial and boundary) and geometrical conditions. As shown in Figure 5, the thermal bubble around the heater changes with changing acceleration. In this study, we observed that with the application of rotation/vibration in addition to acceleration, the thermal bubble around the heater also changed in the direction of the applied motion. The steps involved in measuring multiple physical quantities using a motion sensor are shown in Figure 9.

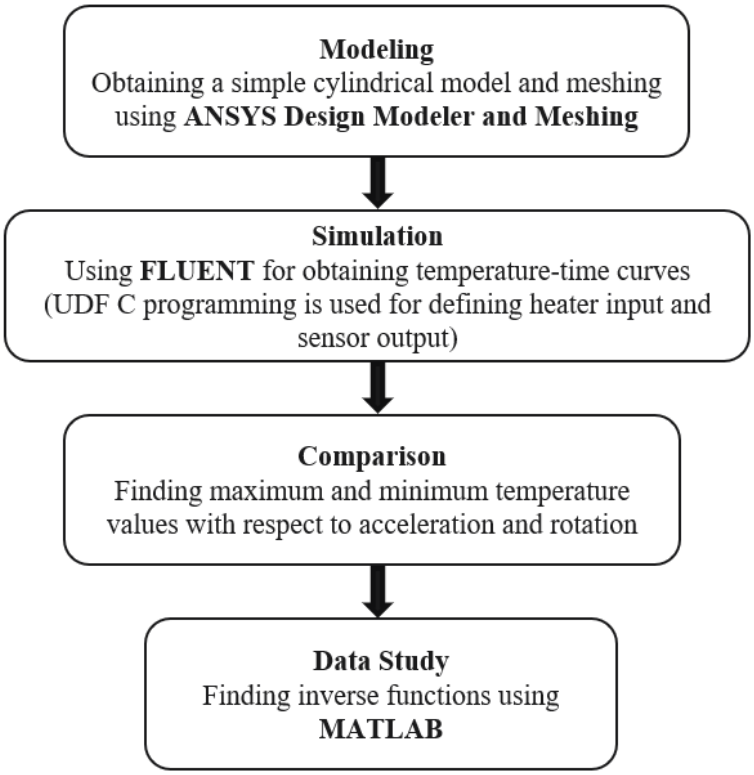

Figure 9- Methodology flow

In this study, we have analysed three different cases and for all these, the flow conditions and parameters vary:

Case 1: Measuring acceleration in the x-direction and rotation around the z-axis.

Case 2: Measuring acceleration in the x-direction and amplitude (of vibration) in the z-direction.

Case 3: Measuring acceleration and rotation in all three directions.

The computational model and mesh for cases 1 & 2 are the same, whereas the design model, as well as the mesh, is different for case 3. The overall procedure for measuring multiple physical quantities in all three cases resembles the process illustrated in Figure 9. These steps are described as follows:

1. Model and mesh generation:

The first step was obtaining a 3D design of the sensor and creating a mesh. For simplicity, the shape of the thermal motion sensor was chosen to be cylindrical in shape which represents the cavity of a real sensor. Inside the cavity, four heating sources were defined that created a thermal bubble around them. Next to each heater, sets of temperature sensors were positioned. The heating sources and temperature sensors, however, were defined by using computer code, therefore, the geometry was essentially just a cylindrical shape. These are described in detail later in section **3.2**. Due to the simple nature of the geometry, ANSYS Design Modeler was utilized for creating the model instead of alternative 3D solid modeling computer-aided software such as SolidWorks. Although SolidWorks is a popular CAD tool because of its wide array of features and variety of functionality, keeping in view the additional cost associated with it, ANSYS Design Modeler was deemed suitable for this task.

The next step, which is one of the most important steps in CFD is the meshing of the model. In this method, the body is divided into small discrete elements or cells. The small elements or cells are then treated as independent bodies and governing equations (Navier's Stokes equation in this case) are applied to them in order to find the numerical solution. For ensuring an accurate and reliable solution, the quality of the mesh needs to be significantly well. The meshing chosen for this study is described in section **3.3**.

2. Simulation to obtain temperature-time curves:

Once we have obtained a well-executed meshing of the model, it was used as an input to the CFD simulation software. In our research study, FLUENT was chosen as the CFD tool, which is developed by ANSYS. One of the special characteristics of FLUENT is that it is fully integrated within the ANSYS Workbench, allowing users to quickly solve specific challenges with great ease [72]. This also enables multi-physics simulation and smooth workflow integration with other ANSYS products.

In FLUENT, using appropriate input and boundary conditions (which are described in section **3.4**), temperature-time curves were obtained. The meshed geometry was accelerated in one direction and rotated/vibrated in another. Due to the convective heat transfer phenomena within the thermal accelerometer, these responses were observed to be periodic in nature, as represented in Figure 10. It can be observed that the periodicity of the curve began after a certain time as the temperature started to rise from room temperature 300K at time 0s. This is known as the time lag between the input physical quantities and the corresponding temperature responses. This may vary depending on the thermal conductivities of the material involved.

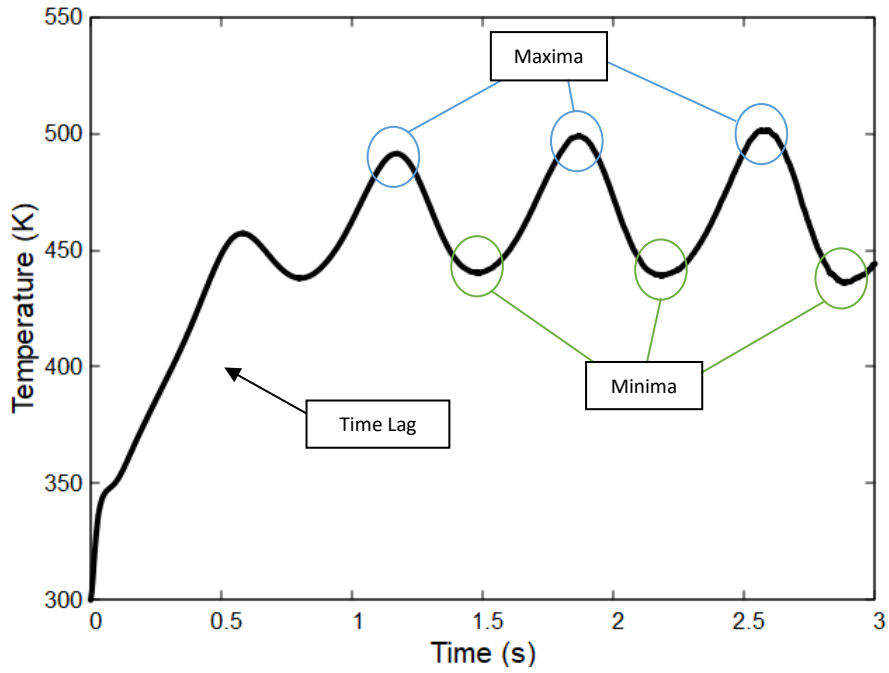

Figure 10- Temperature-time curve illustration

From the temperature-time curves, the output values were extracted which are then correlated with the input physical quantities. For case 3, output values were simply the extreme values (maxima and minima) from temperature sensors surrounding the heaters. For case 1 and 2, on the other hand, output values were obtained by first generating temperature-time curves of two equidistant sensors from the heaters, subtracting the two graphs, and then obtaining maxima of that graph. Since the temperature response of the two graphs was periodic, the temperature difference-time graph was also a periodic curve as the one represented in Figure 10, except for changing the y-label from temperature (T) to temperature difference (ΔT).

3. Comparison: Obtaining output values

Since there was a correlation between the T_{max}/T_{min} and ΔT_{max} values with the input physical quantities, by inputting different values of acceleration and rotation/amplitude of vibration to FLUENT, sets of data were obtained. Case 1 listings are presented in Table 8 and Table 9, for case 2 in Table 10 and Table 11 and data for case are noted in Table 12, Table 13 and Table 14.

4. Finding Inverse Function

The general method can be described as follows. The idea is to define a relationship between multiple physical quantities (PQ) that we are interested in and multiple outputs by computational simulations, as generalized below:

$$\left(\text{Output 1}, \text{Output 2}\right) = f\left(\text{PQ 1}, \text{PQ 2}\right)$$

For each value of a physical quantity, there is a corresponding set of outputs. However, the number of outputs should be the same as the number of physical input quantities. Therefore, cross-axis sensitivity is useful as an input physical quantity applied around one axis, can be measured using output data at another axis. Once this relation has been obtained, the next step is to determine the inverse function of this relationship as:

$$\left(\text{PQ 1}, \text{PQ 2}\right) = f^{-1}\left(\text{Output 1}, \text{Output 2}\right)$$

To present the data from the above equation, a 3D plot needs to be drawn, one for each physical quantity such that the two outputs are plotted on the x and y-axis, and the corresponding physical quantity is plotted on the z-axis. It is to be noted, however, that the basic principle of natural convection of the thermal motion sensor for all three cases is the same. Therefore, the governing equations predicting the response were similar for this study and it is described in detail in the next section.

3.1 Governing Equations

A computational simulation was performed to observe natural convection, and changes in the temperature profile as acceleration and rotational speed/vibration were simultaneously applied to the computational model. The governing equations for predicting the temperature profile of our thermal motion sensor are based on the principle of conservation of mass, momentum, and energy, which are as follows:

$$\frac{\partial \rho}{\partial t} + \nabla . \left(\rho \mathbf{u}\right) = 0$$

$$\rho\left(\frac{\partial \mathrm{u}}{\partial \mathrm{t}}\right)+\mathrm{u}.\nabla\,\mathrm{u}=-\nabla \mathrm{p}+\nabla.\mathrm{I}+\mathrm{f}$$

$$\rho C_p\left(\frac{\partial \mathrm{T}}{\partial \mathrm{t}}+\mathrm{u}.\nabla \mathrm{T}=\mathrm{k}\nabla^2\mathrm{T}\right)$$

where *u* is the flow velocity vector field, ∇ is the spatial divergence operator, p is the pressure, I is the total stress tensor, and f denotes the body forces acting on the fluid. The parameters C_p, ρ, and k are the specific heat, density, and thermal conductivity, respectively, of the fluid in the cavity.

The computational fluid dynamics package FLUENT was employed for the analysis using the finite-difference method to discretize the governing equations shown above.

3.2 Geometrical Dimensions and Motion Types

Case 1:

A simple cylindrical geometry, representing the cavity of a real thermal motion sensor, was considered for the analysis with 1 cm of height and a diameter of 2 cm. As shown in Figure 11, four temperature sensors (black dots) adjacent to the four edges of rectangular heaters (red rectangle) were considered. A double-axis thermal accelerometer was considered in this case. All four heaters lay on every axis and were placed 0.4 cm from the center of the cavity. The distance between heaters and sensors was set to be 0.0537 cm. The reason for choosing this value has been described in section **4.1.2**.

The size and power of our target model were determined as follows: in the literature, different scales of Unmanned Aerial Vehicles (UAVs) have been studied to achieve lighter weight and lower lifting and sensing power. Kevin [73] built an 80 mg, insect-scale, flapping-wind robot with a power consumption of 19 mW. Another study specifies the lifting and sensing power to be 100 mW for an insect-scale UAV with a mass of 100 mg [74]. Therefore, keeping this in view, our target model consists of a device with dimensions of 1 cm (height) and 2 cm (diameter) with a heating power of 70 mW for application in small-scale UAVs and robots.

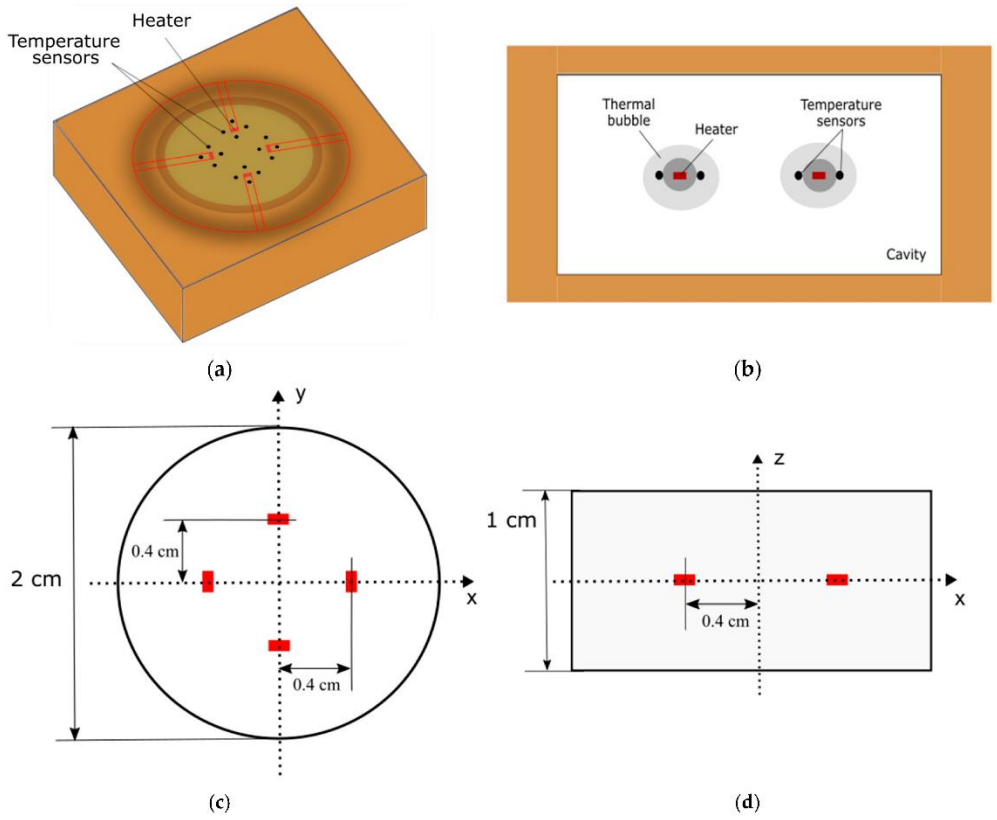

Figure 11- Model illustration: (a) isometric view; (b) side view and geometric dimensions: (c) cross-section view; (d) side view.

Heaters and temperature sensors are incorporated into this design using user-defined functions (UDFs). In the UDFs, the locations of heaters and sensors are defined and tracked using their cell IDs, which are unique for every cell, even when the geometry is moving. Instead of tracing the coordinates of heating sources, the cell IDs of cells containing the heating sources are traced to determine the centroid location of these coordinates (**Appendix A**). In addition, using the 'DEFINE_SOURCE' UDF, heat is applied to the cells where the heat sources exist. Furthermore, temperature values are extracted by looping over the entire cells and locating the cell IDs of sensors (**Appendix B**).

For case 1, rotation around the center of the cylindrical device in the counterclockwise direction (*z*-direction) and acceleration in the negative *x*-direction were applied simultaneously, as shown in Figure 12. Four heating sources (red squares, numbered 1-4) were placed at various positions, and each heating source was surrounded by four temperature sensors (circles in four colors) in the *x*- and *y*-directions. As the device is accelerated and rotated simultaneously in space, each temperature sensor provides a unique temperature profile that changes with time. Sensors with the same color generate similar temperature responses. The sensor denoted *X21* is the *x*-

sensor around Heater 2 in the positive direction (orange circle). Similarly, *Y42* denotes the *y*-sensor around Heater 4 in the negative direction (purple circle). From Figure 12, any set of one selected heater with its four surrounding sensors out of the four sets can be considered for the analysis. All sensors were placed equidistant from the heaters.

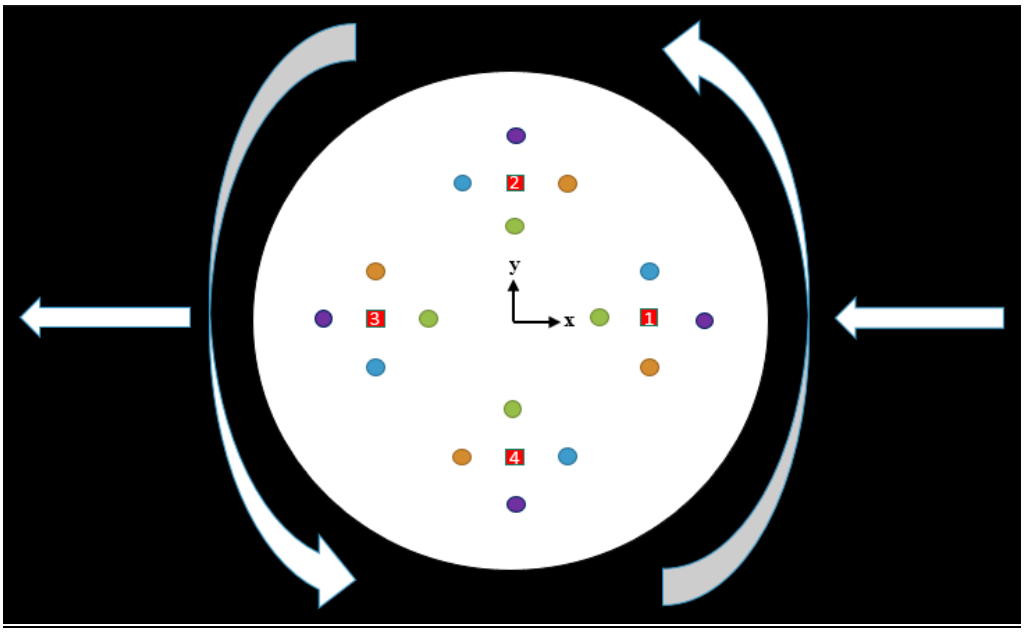

Figure 12- Direction of motion and position of heaters and sensors for case 1.

Case 2:

For case 2, similar geometrical dimensions of the cavity and heaters were considered as case 1. However, instead of X and Y sensor data, X and Z sensors were analyzed. The position of heaters and sensors is shown in Figure 13.

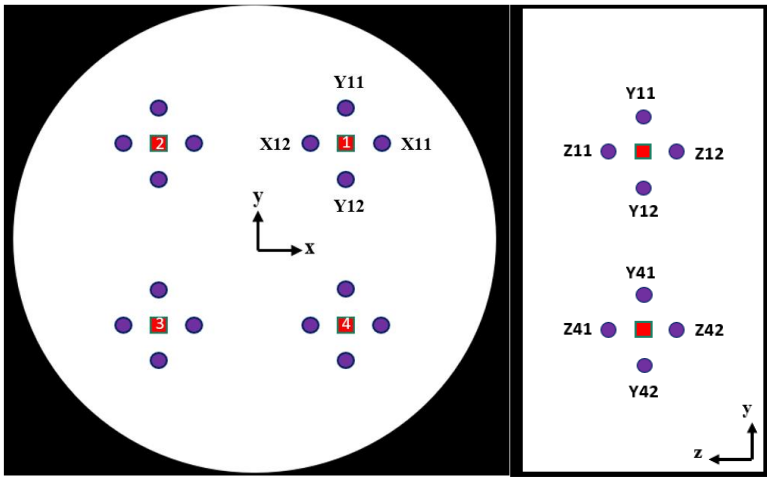

Figure 13- Position of heaters and sensors; cross-sectional view (left) and side view (right) for case 2.

Here, we have *x*-acceleration and *z*-amplitude as the two input physical quantities, whereas the response obtained at sensors around heater 1 i.e. ΔT_X_{max} and ΔT_Z_{max} as the two outputs which are defined by:

$$\Delta T\_X_{max} = T\_X11 - T\_X12$$

$$\Delta T\_Z_{max} = T\_Z11 - T\_Z12$$

Considering the other heater positions with their four surrounding sensors, similar results should be generated. For measuring the frequency of vibration, the temperature response at a single sensor location is obtained to be at the same frequency as the input z-vibration.

Case 3:

In this case, acceleration and rotational speeds were measured in all three directions. Therefore, a triple-axis thermal motion sensor needed to be considered here. The design and geometrical dimensions of the sensor were altered. The placement of the heaters and sensors is shown in Figure 14. Four heaters (*H1–H4*) were placed on all four axes, 40 mm from the center of the cavity. Heaters *H1* and *H3* on the *x*-axis are surrounded by pairs of *x*-sensors *X21* and *X22*, and *X11* and *X12*, respectively. Similarly, *H2* and *H4* on the *y*-axis are bounded by *y*-sensors *Y21* and *Y22*, and *Y11* and *Y12*, respectively. On the *z*-axis, each heater constitutes a temperature sensor located 10 mm away from the heater in the *z*-direction. The notation of the *z*-sensors is such that the number denotes the heater number (e.g., *Z1* around *H1*).

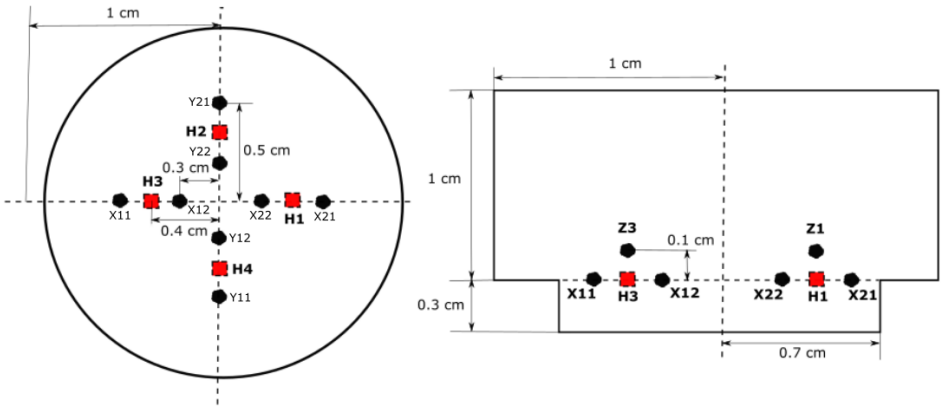

Figure 14- Position of heaters and sensors; cross-sectional (left) and side views (right) of a triple-axis thermal motion sensor (for case 3).

At this point in our research, we have established the notion that it is possible to measure two physical quantities simultaneously using this particular method. In this case, this relationship is obtained for two quantities in three directions. Therefore, six inverse functions must be obtained, and the data can be installed in the computing unit of the motion sensor. This is illustrated in Figure 15.

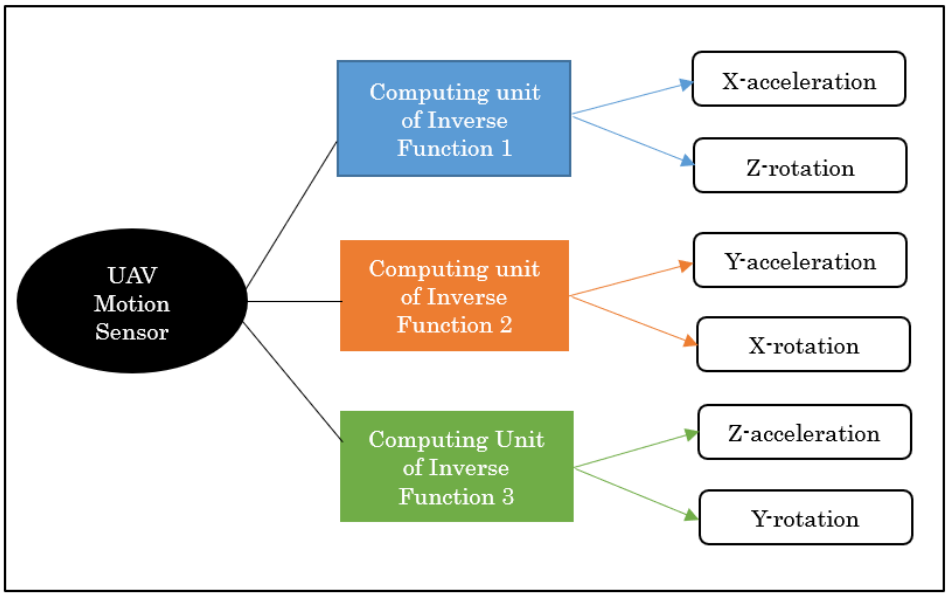

Figure 15- Schematic of obtaining three inverse functions for the measurement of acceleration and rotation in all three directions.

For the material of the computational domain surrounding the cavity for all three cases, polyvinylidene fluoride (PVDF) and polyimide were chosen to be best suited because of their good thermal heat resistance with high values of specific heat capacity (C_p) and low values of thermal conductivity (k), as listed in Table 4.

Table 4- Mechanical properties of MEMS materials.

Material	*Thermal Conductivity (W/m/K)*	*Specific Heat Capacity (J/kg/k)*	*Density (kg/m³)*
PVDF	0.2	1500	1780
Polyimide	0.1	1100	1420

3.3 Meshing Method

The ANSYS Fluent meshing method effectively applies the element size to any given face or group of faces, ensuring a consistent, high-quality mesh size for the region. As described in the previous section, a dual-axis thermal sensor was considered for case 1 & 2 where two physical quantities were measured simultaneously (*x*-acceleration and *z*-rotation & *x*-acceleration and *z*-amplitude of vibration). On the other hand, a triple-axis thermal sensor needed to be considered for case 3 where two quantities (acceleration and rotation) were measured in all three directions. The meshing parameters for cases 1 & 2, therefore, were different from case 3.

3.3.1 Dual-axis Thermal Sensor Mesh

An optimal grid design is required to obtain accurate results with a reduced computational time. To achieve this, we employed the grid resolution method proposed by Minhyung [75] and created a computational grid, as shown in Figure 16, using the meshing software in ANSYS 18.2. The number of elements and nodes of this structure are 310,947 and 1,283,732, respectively.

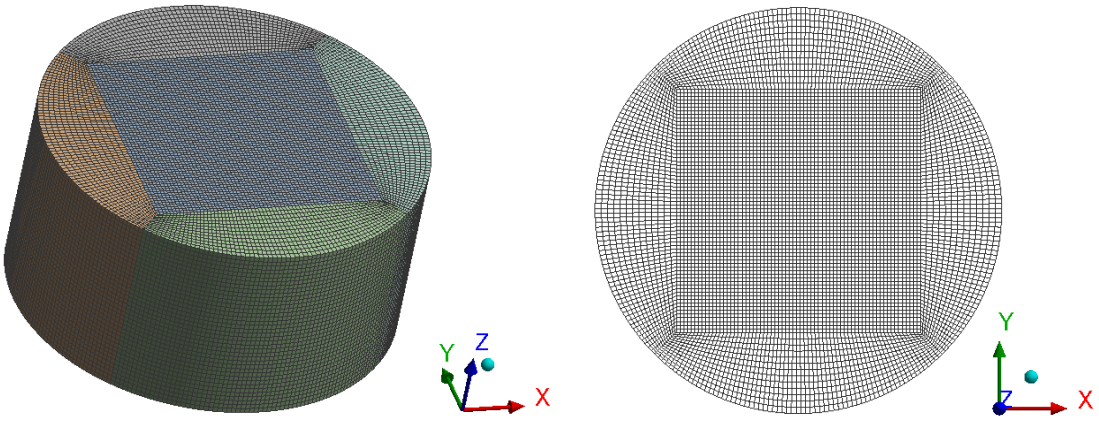

Figure 16- Computational mesh; isometric view (left) and wireframe top view (right) for cases 1 & 2.

Checking quality of the mesh is essential for ensuring reliable and accurate simulation results. This was checked here by looking at element quality and aspect ratio of the generated mesh.

3.3.1.1 Element Quality

The element quality is a composite quality (range from 0 to 1), as shown in the equation below [76]:

$$\text{ELEMENT QUALITY} = C\left[\frac{\text{Volume}}{\sqrt{\left(\sum(\text{Edge Length})^2\right)^3}}\right]$$

where the element determines the value of *C* which is a constant value. Element quality is the ratio of the volume to the square root of the cube of the sum of the square of the edge lengths. If it is 1, it is a perfect square. From the ANSYS Fluent numerical results, most of the element quality of this experiment is close to 1 as shown in Figure 17.

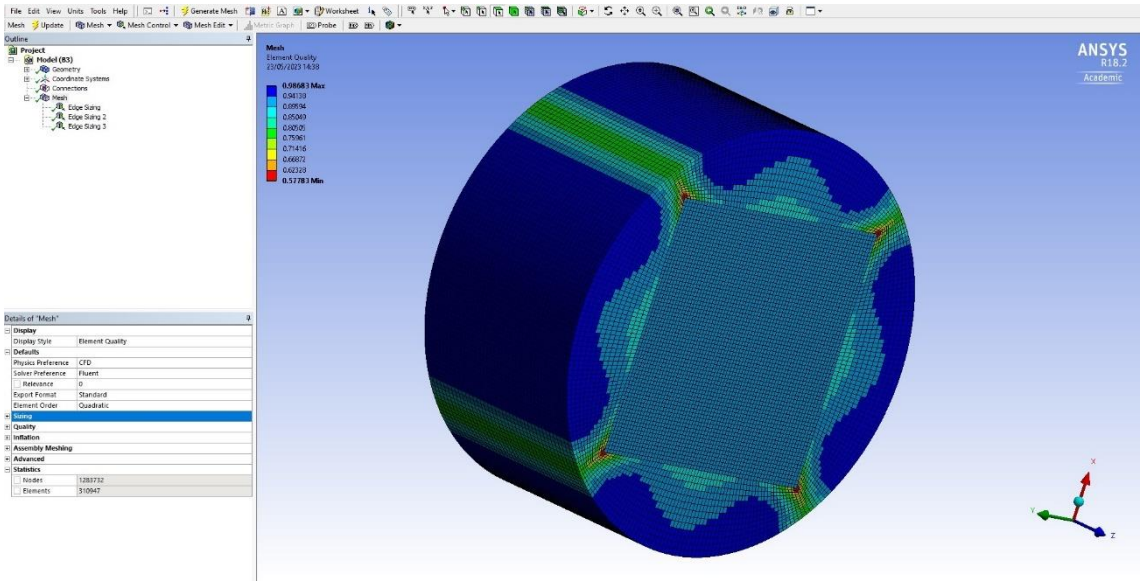

Figure 17- Element quality of the dual-axis thermal motion sensor.

3.3.1.2 Aspect Ratio

Aspect ratio is the deviation of the component when the length of each side is equal, as shown in the equation below [77]:

$$\text{ASPECT RATIO} = \frac{\text{Long Edge Length}}{\text{Short Edge Length}}$$

As shown in the above equation, the aspect ratio value must be about 1. If the ratio is 1, the shape is a perfect square, and the shape will be distorted if the ratio becomes larger. So, a value closer to 1 means a better quality of meshing. From the ANSYS numerical results, most of the aspect ratios of this experiment are below 2.5 and close to 1 as shown in Figure 18.

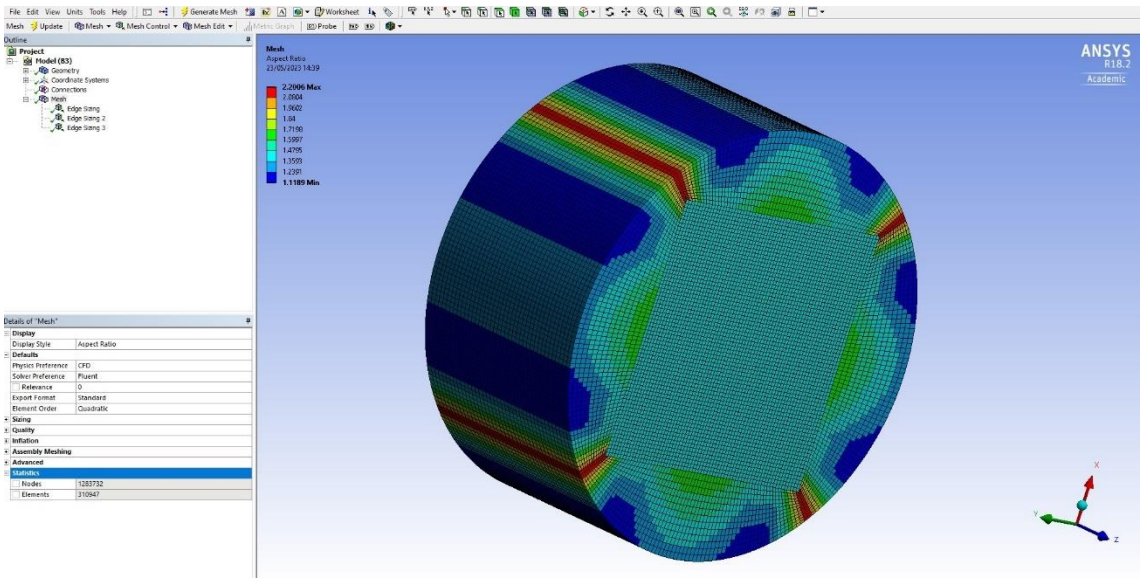

Figure 18- Aspect ratio of the dual-axis thermal motion sensor.

3.3.2 Triple-axis Thermal Sensor Mesh

A mesh using quadrilateral elements was also chosen for the tri-axial thermal sensor. The geometry and dimensional constraints were set up as defined earlier in Figure 14, which was different than the double-axis sensor because of the installation of *z*-sensors. In the previous case, a mesh consisting of 310,947 elements were chosen, which required a reasonable amount of time to conduct the simulations. In this case, we wanted to test the mesh in a manner that yields results with a reduced computation time while minimizing CPU power consumption. Moreover, to validate the reliability and independence of computational simulation results, a grid-independence test was conducted because no experimental or theoretical models were available for comparison.

3.3.2.1 Mesh Independence Test

The velocity, pressure (at sensor *X11*), and temperature variables were evaluated at 500°/s around the *z*-axis, and 2*g* was applied to the device in the *x*-direction using five different

meshes with varying numbers of elements. The velocity and pressure distributions (viewed from the top plane of the motion sensor) of a mesh with 166,675 elements are shown in Figure 19. It can be observed that the velocity of CO_2 molecules was practically the same throughout the motion sensor cavity with a maximum velocity of 49.23 m/s^2 at the instant of t = 2.5 s. Furthermore, the temperature change with respect to time for all five meshes is shown in Figure 20. The maximum values in this graph were extracted and used for comparison.

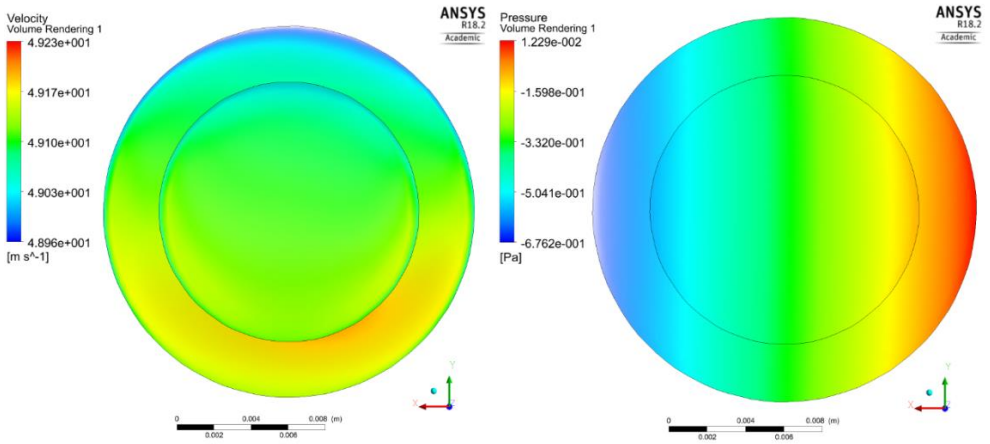

Figure 19- Velocity (left) and pressure distribution (right) at t = 2.5 s for the mesh with 166,675 elements.

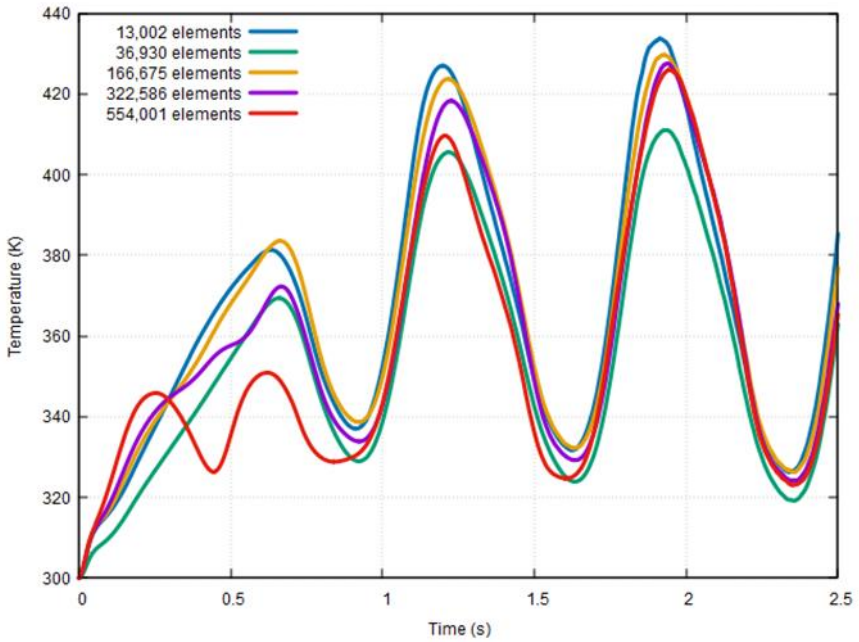

Figure 20- Temperature response at 500°/s around the Z-axis and 2g applied in the X-direction for different mesh sizes.

The results of the grid-independence test are presented in Table 5 and illustrated in Figure 21 by comparing the T_{max} values with respect to the number of mesh elements.

Table 5- Change of variables with changing mesh elements.

S#	No. of Mesh Elements	V_{max}(m/s)	P_X11$_{min}$ (Pa)	P_X11$_{max}$ (Pa)	T_{max} (K)
1	13,002	49.23	-0.497392	-0.168213	433.7
2	36,930	49.23	-0.509235	-0.167053	411.0
3	166,675	49.235	-0.508066	-0.181941	429.8
4	322,586	49.235	-0.513125	-0.183977	427.5
5	554,001	49.24	-0.518651	-0.185735	426.0
6	752,760	49.16	-0.523673	-0.186014	421.6

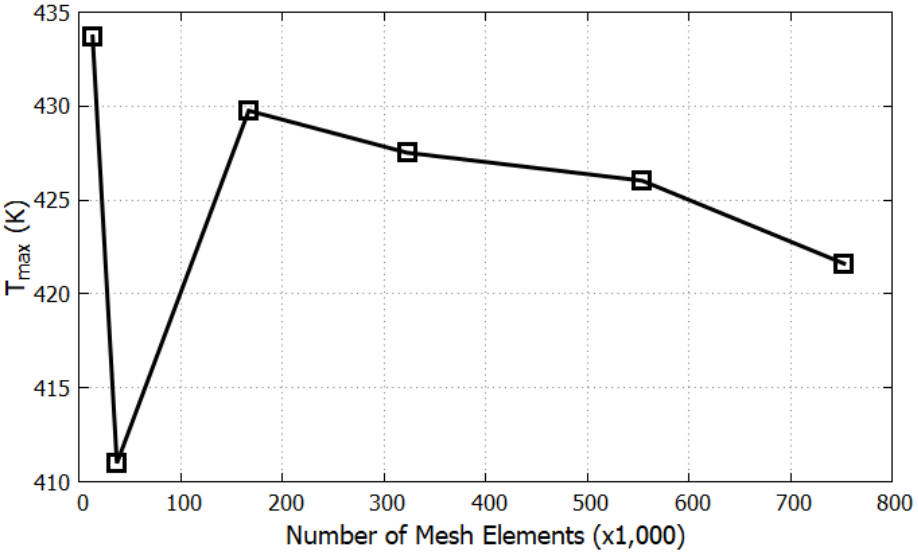

Figure 21- T_{max} vs number of mesh elements.

It can be observed in Figure 21 that a significant increase of 4.6% in the T_{max} value is observed between the second and third meshes. However, from the third mesh onwards, the difference in T_{max} values between the meshes is about 1%, which is minimal compared to the first three. As a result, the mesh with 166,675 elements was chosen for future calculations, as it provides a reliable solution with minimal computational requirements such as CPU time. This is shown in Figure 22.

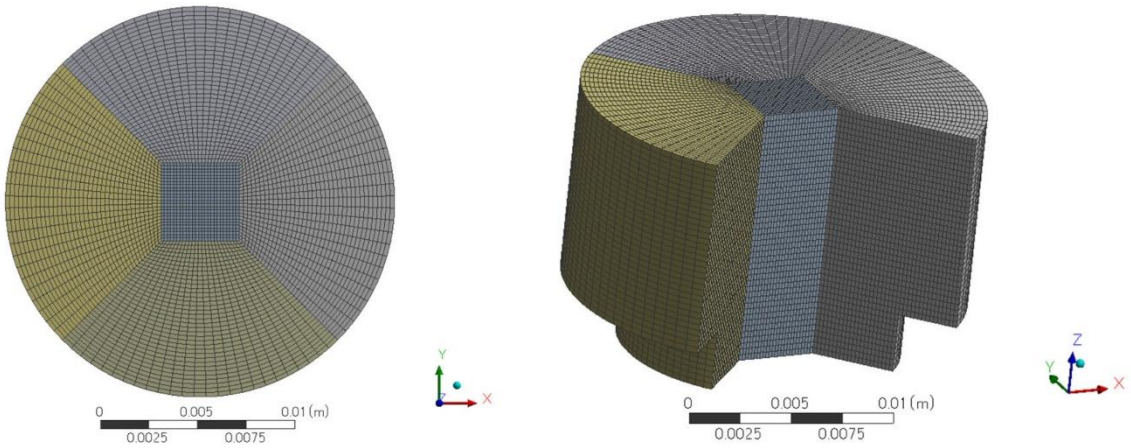

Figure 22- Computational mesh of the triple-axis motion sensor; top view (left) and isometric view of the inside of the mesh (right).

3.3.2.2 Element Quality and Aspect Ratio

Once a mesh is designed, and its independence from certain parameters is verified, it is important to check the element quality and aspect ratio of the mesh elements such that satisfactory results could be drawn from it. The element quality and aspect ratio of the mesh from Figure 22 are shown below in Figure 23 and Figure 24.

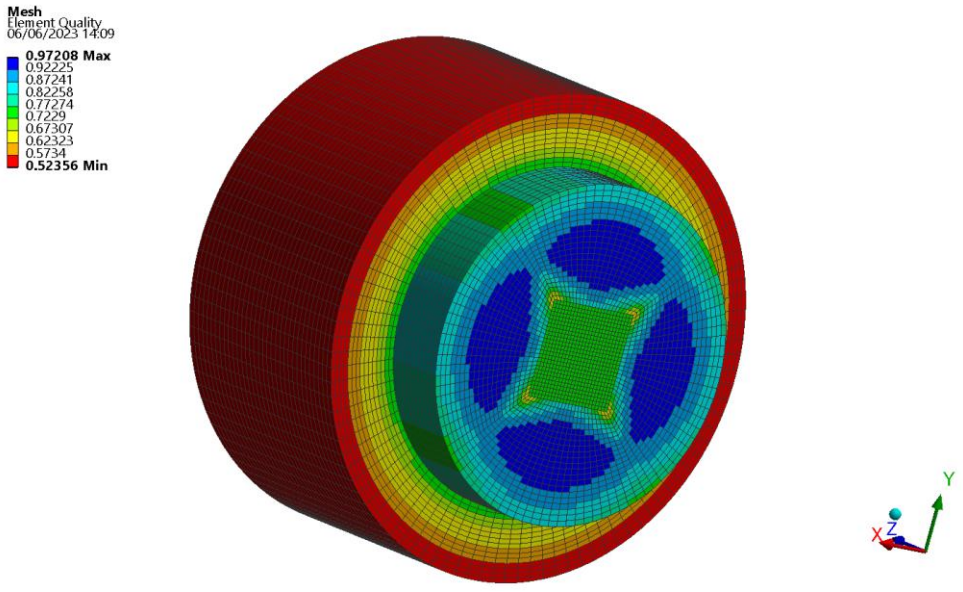

Figure 23- Element quality of the triple-axis thermal motion sensor mesh.

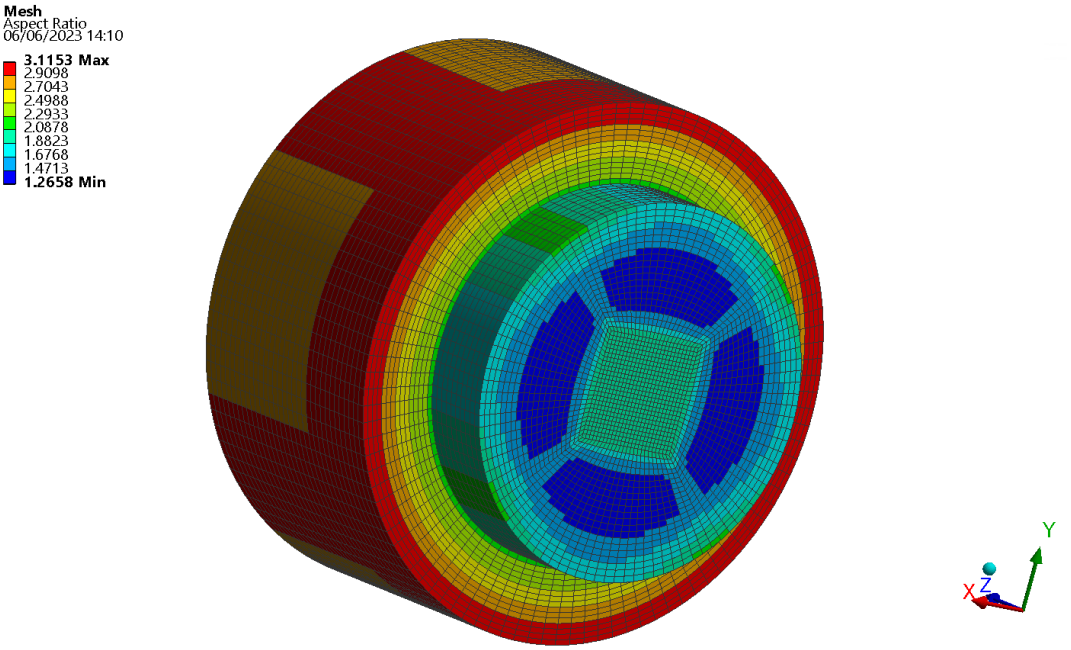

Figure 24- Aspect ratio of the triple-axis thermal motion sensor mesh.

It can be observed from the above figures that the mesh elements around the outer boundary of the sensor have lower quality (52.36%) and a higher aspect ratio of 3.12. This is acceptable because the heaters and sensors are placed towards the center of the cylinder where quality of the mesh was in the good range. The quality could be further increased if smaller mesh elements were considered, however, our goal was to reduce the computation time, this is overall acceptable.

3.4 Flow Conditions and Parameters

For the simulations, a time step size of 0.0042 s was considered keeping in view increment velocities. For case 3, the acceleration and rotation ranges were set to be 1–4*g* and 250–1000°/s. For the case of acceleration, the maximum velocity for a flow time of 3 s was 117.72 m/s with an increment velocity of 0.164808 m/s at 4*g*. In contrast, for rotational velocities, a maximum linear speed of 0.174533 m/s was practically the same as the maximum increment velocity at 4*g*. The values are listed in Table 6 for comparison.

Table 6- Maximum and increment velocities at different accelerations and rotations.

		Maximum velocity at 3 s (m/s)	Increment velocity (m/s)
Acceleration	1g	29.43	0.0412
	2g	58.86	0.0824
	3g	88.29	0.1236
	4g	117.72	0.1648
Rotation (°/s)	250	0.0436	0.0436
	500	0.0873	0.0873
	750	0.1309	0.1309
	1000	0.1745	0.1745

In FLUENT, a pressure-based transient solver was used along with an energy model because the flow characteristics were not highly compressible with a lower Mach number. Regarding the gas medium, carbon dioxide (CO_2) was selected because of its high density and low kinematic viscosity. The low viscosity of CO_2 enables a more efficient flow and results in greater sensitivity than gases with higher viscosities because high viscosity impedes gas flow [68]. In section **4.1.3**, a comparative study has been presented to determine the better gas medium amongst Air, CO2, and N2. Moreover, in section **4.1.2**, a comparison has also been drawn to determine the optimal distance between heaters and sensors (0.0537 cm).

In thermal accelerometers, a heating source that generates temperature contours must be defined. The temperature response is generally greater when the heating power is high, and the ambient temperature is low. Therefore, differences in peak values increase. However, this results in higher temperatures inside the cavity, which can lead to the heating of the motion sensor walls. As explained earlier, a heating power of 70 mW was applied in response to the device's intended applicability to small-scale UAVs that require low sensing and lifting powers for case 1 & 2. In case 3, however, we further reduced the heating power from 70 to 40 mW such that it can be applied to significantly smaller UAVs. These simulation parameters are listed in Table 7.

Table 7- Simulation parameters

S#	Simulation parameters	Parameters value
1	Software	ANSYS FLUENT
2	Solver type	Transient
3	Model type	Energy
4	Gas medium	CO_2
5	Distance between heater & sensors	0.0537 cm
6	Heater power	70 mW (case 1 & 2), 40 mW (case 3)
7	User-Defined functions	DEFINE_CG_MOTION DEFINE_SOURCE DEFINE_EXECUTE_AT_END

Chapter 4: Results

By employing the methodology described in **Chapter 3**, we have achieved the goal of measuring multiple physical quantities for three different cases.

4.1 Measuring X-acceleration and Z-rotation

A dual-axis thermal motion sensor was employed to achieve the goal of measuring X-acceleration and Z-rotation simultaneously. The computational model used for this study is illustrated in Figure 11 and the position of heaters and sensors along with the direction of motion is shown in Figure 12.

4.1.1 Measuring Maximum Temperature Difference Values

As described in **Chapter 3**, a relationship needs to be obtained between the output values and input physical quantities. In this case, acceleration in the x-direction and rotational speed around the z-axis are the two inputs. Corresponding to these inputs, two output values needs to be determined and measured such that a relationship can be created. In the FLUENT software, the temperature-time responses are observed to be periodic in nature. We observed different temperature responses (temperature-time curves) when different combinations of acceleration and rotation are applied simultaneously. For demonstration, Figure 25 shows the temperature responses at *Y31* and *Y32* sensors around heater 3 (orange and blue) when an acceleration of 27.42 m/s^2 (3*g*) and a rotational speed of 12.57 rad/s (3π) are applied simultaneously.

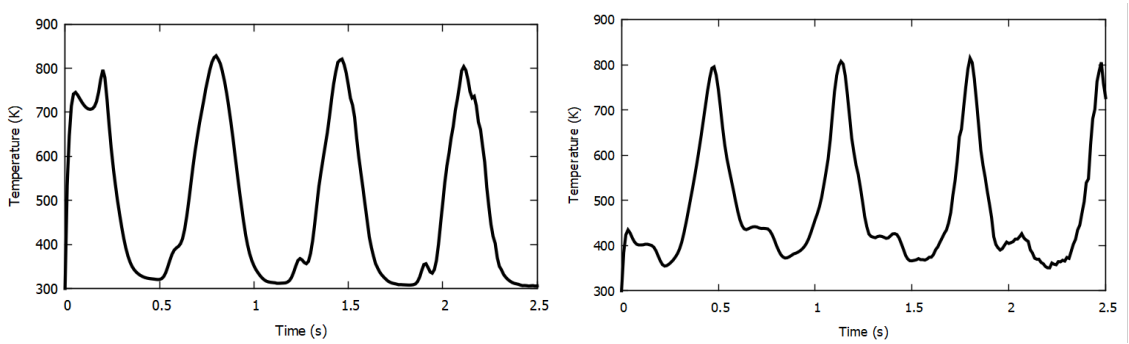

Figure 25- Temperature response of sensor Y31 (left) and sensor Y32 (right) at 3g and 3ω.

In this study, we have analysed the simultaneous application of *x*-acceleration ranging from 9.81 m/s^2 to 39.24 m/s^2 (1*g*-4*g*) and rotational speeds from 6.28 rad/s to 15.71 rad/s (2π-5π rad/s). For extracting output data, we have considered the temperature difference values (*T_Y32 – T_Y31*) between the pair of sensors equidistant from the heater. These values are

different for different input physical quantities because of natural convection. As the temperature response of all sensors is periodic, ΔT w. r. t. time is also periodic and maximum temperature values (maxima) are extracted from the graph, as the output values. For our analysis, we considered the results of the sensors around Heater 3, other heater positions and the surrounding sensors should also generate similar plots. These temperature sensors are denoted *X31*, *X32*, *Y31*, and *Y32* (green, purple, orange, and blue in Figure 12), and the maxima of the temperature differences of the X and Y sensors are represented as ΔT_X_{max} and ΔT_Y_{max}, respectively.

To visualize the above-mentioned method, we display the temperature responses at sensors *Y32* and *Y31* at a fixed rotational speed of 4π and varying accelerations of 1*g*, 2*g*, 3*g,* and 4*g* in Figure 26. The next step involved obtaining the difference between these two temperature responses, represented by *T_Y32 – T_Y31*, as shown in Figure 27.

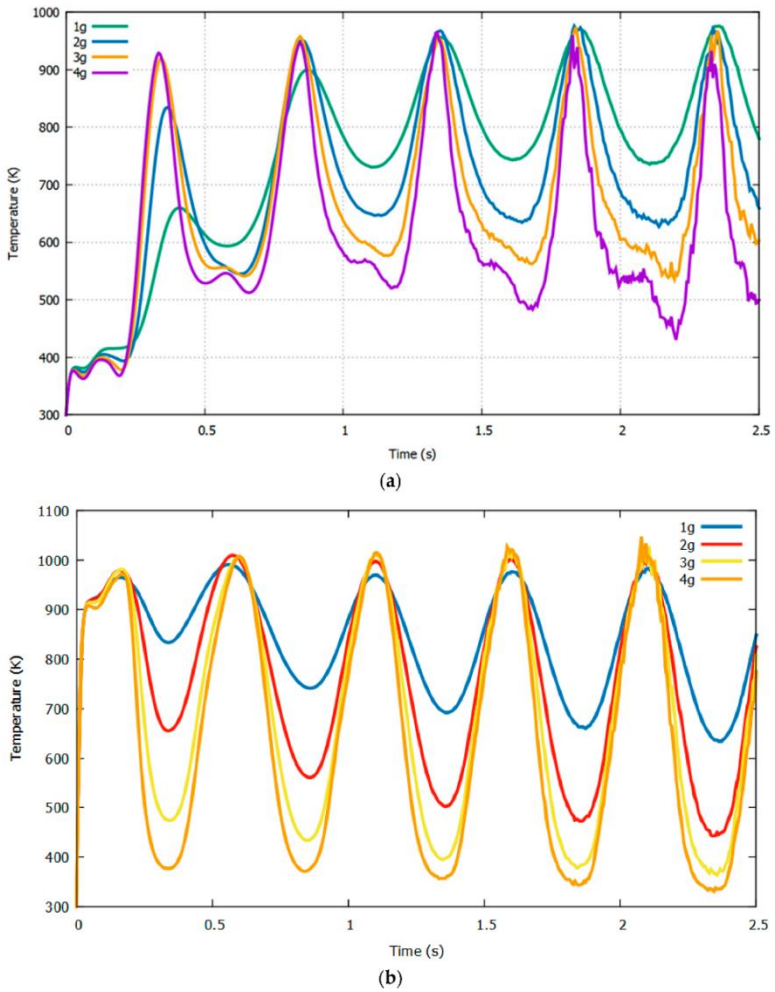

Figure 26- Temperature response of sensors Y32 (a) and Y31 (b) at 4π rad/s with varying acceleration.

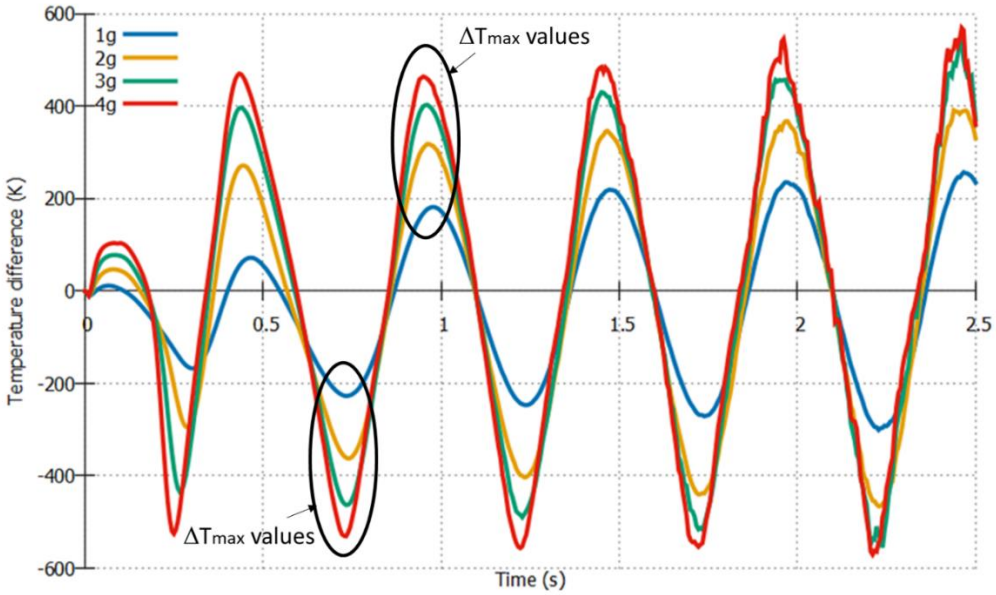

Figure 27- Temperature difference between sensors Y32 and Y31 w.r.t time at 4π rad/s with varying acceleration.

From Figure 27, we have evaluated maximum temperature values in determining ΔT_Y_{max}. These maxima values change depending on simulation conditions and parameters, and directly influence the sensitivity of the device. Therefore, to improve the sensitivity, we have studied the effects of changing the distance between the heater and sensors and changing the gas medium on the maximum temperature difference values (ΔT_{max}). At 1*g*, 2*g*, 3*g*, and 4*g* with a constant rotation of 4π rad/s, we have obtained ΔT_{max} values of 238.60852K, 389.7796K, 523.474K, and 575.5737K, respectively.

4.1.2 Study of the Effect of Changing Distance Between Heater and Sensors

To see how changing the distance between heater and sensors affects maximum temperature difference values (ΔT_X_{max} and ΔT_Y_{max}) and how the performance parameters can be improved, we have considered six different positions of temperature sensors by changing the distance from the heater to 0.0179 cm, 0.0358 cm, 0.0537 cm, 0.0896 cm, 0.1254 cm, and 0.1433 cm. Through these simulations, a suitable distance was found.

For those six different positions of the sensors, the ΔT_Y_{max} values extracted at a constant rotational speed of 4π rad/s and increasing acceleration from 1*g* to 4*g* are shown in Figure 28, and those at a constant acceleration of 3*g* and increasing rotation speed from 2π to 5π rad/s are shown in Figure 29.

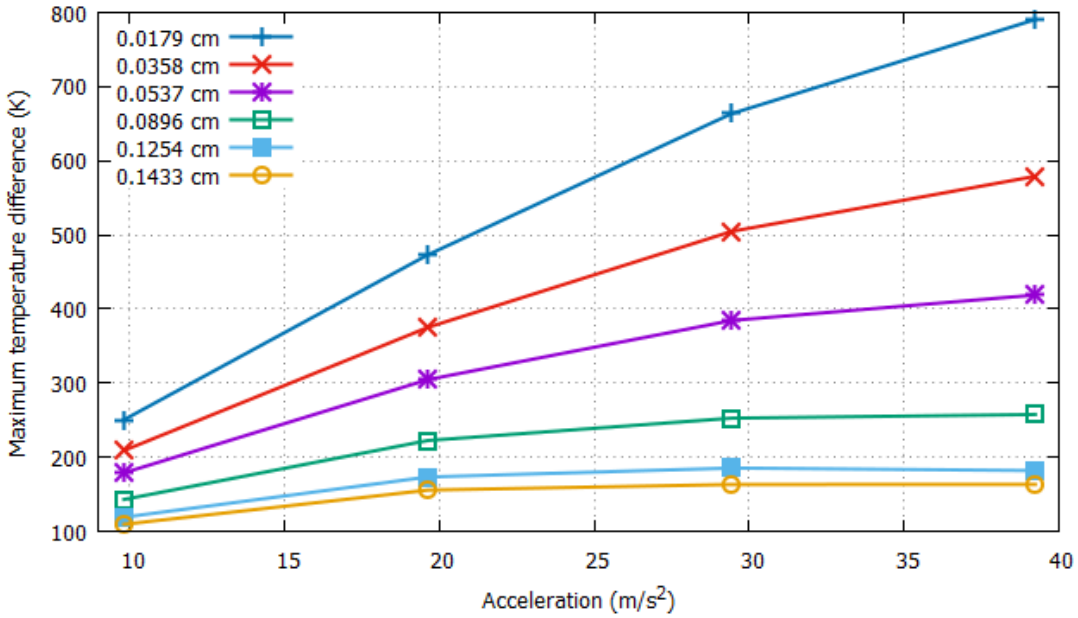

Figure 28- ΔT_Y_{max} w.r.t acceleration at 12.57 rad/s with varying distance between heater and sensors.

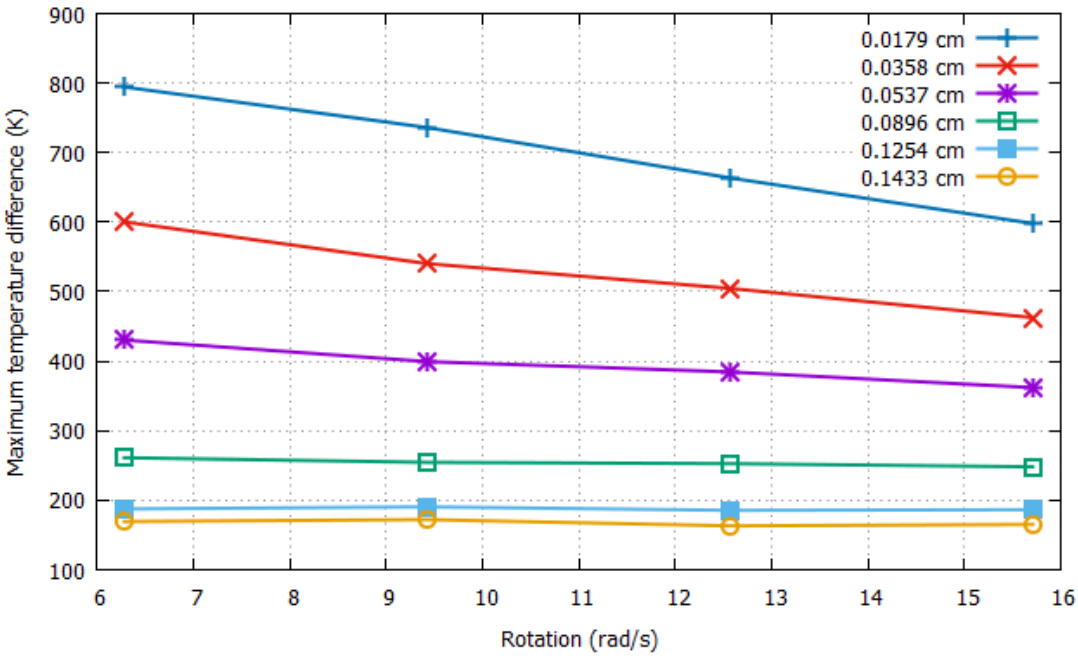

Figure 29 - ΔT_Y_{max} w.r.t rotation at 3g with varying distances between heater and sensors.

From Figure 28, it can be seen that maximum temperature difference (ΔT_{max}) values are observed to be higher as the distance between heater and sensor is lower. The information that can be extracted from the graph is how these values change by changing acceleration. For 0.0179 cm distance between heater and sensor, when the acceleration was changed from 2*g* to 3*g*,

ΔT_Y_{max} increased from 473.1 K to 663.5 K, resulting in a difference in ΔT_Y_{max} of 190.4 K. Whereas, for the case of a larger distance, i.e., 0.0896 cm, the temperature difference dropped to 30.0 K. This means that for acceleration, shorter the distance is, better the results (sensitivity) are.

In Figure 29 with increasing rotation, we can see that as the distance between heater and sensors is increased, the sensitivity decreases to a point that almost straight lines in the graph are observed. In addition to sensitivity, resolution which is defined as the difference in the output value in response to the input change has also been observed to be reduced by the increased distance between heater and sensors. Between 3π rad/s and 4π rad/s, ΔT_Y_{max} values for the case of 0.0358cm are observed to be 540.4 K and 504.6 K, respectively, which gives a difference of 35.8 K as opposed to 5.0 K for a longer distance as 0.1254 cm between heater and sensors. Thus, a shorter distance between heater and sensors generates better sensitivity and resolution for changing rotational speeds.

Therefore, it can be concluded from Figure 28 and Figure 29 that, as the distance between heater and sensor reduces, better sensitivities and resolution are observed for both acceleration and rotation. In addition to that, we have also observed the *uniqueness* of the solution for all six distances for changing accelerations. On the other hand, for changing rotational speeds, we observed *uniqueness* from 0.0179 cm to 0.0896 cm distance between heater and sensors.

4.1.3 Study of the Effect of Changing Gas Medium

Another crucial parameter that can significantly alter the quality of results is choosing the right gas media for the thermal motion sensor. As described in section **2.6**, sensitivity of the thermal motion sensor is related to the density and viscosity of the gas medium, which means by varying these properties can vary the performance of the device. The proportionality is shown in the equation below:

$$\text{Sensitivity} \propto \frac{\text{Density}}{\text{Viscosity}}$$

To study the effect of changing gas medium, we have considered three different gas mediums, Air, N_2, and CO_2. Their physical properties are listed previously in Table 2. For computational simulations, we have considered heater 3 with its four surrounding temperature

sensors (Figure 25). The distance between the heater and sensors was set to be a medium value of the preceding simulations as 0.0537 cm. The simulation results of ΔT_Y_{max} w.r.t acceleration at 3*g* and rotation at 4π rad/s are plotted in Figure 30 and Figure 31, respectively.

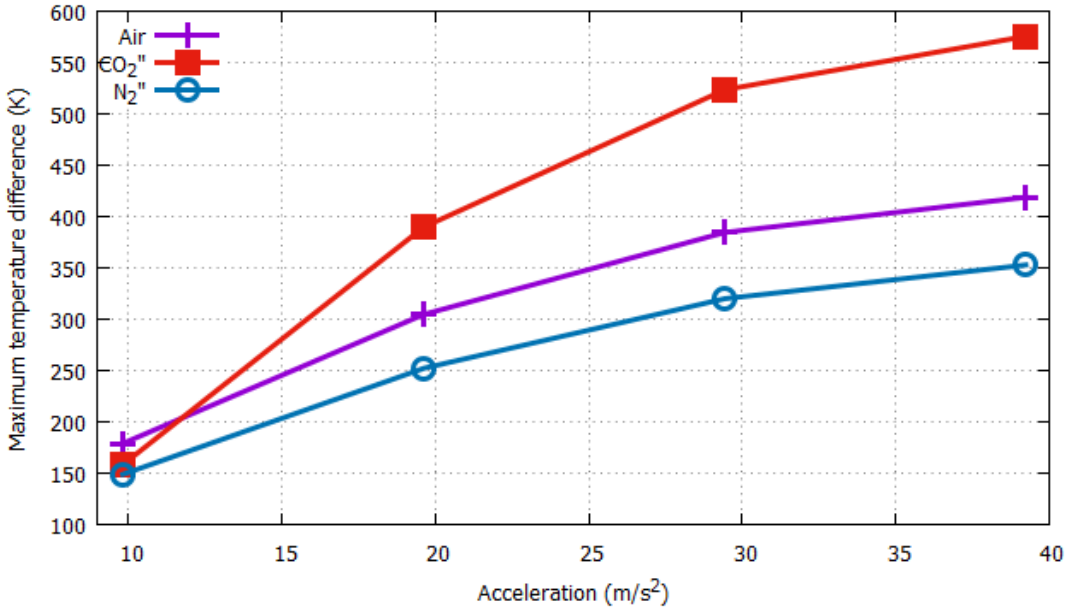

Figure 30- ΔT_Y_{max} w.r.t acceleration at 12.57 rad/s with varying gas media.

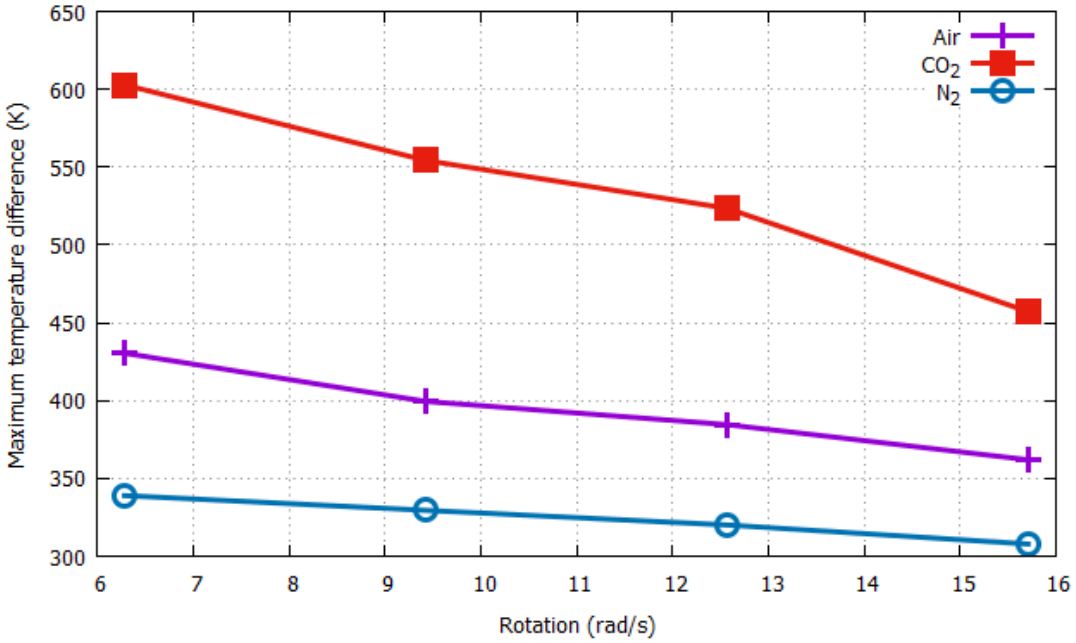

Figure 31- ΔT_Y_{max} w.r.t rotation at 3g with varying gas media.

It can be seen from Figure 30 and Figure 31 that as expected the gas medium CO_2 generated maximum sensitivity and resolution for both changing acceleration and rotation. In Figure 30, as acceleration is increased from 3*g* to 4*g*, the ΔT_Y_{max} value jumps from 523.5 K to 575.6 K resulting in a difference of 52.1 K, as opposed to N_2 with a difference of 32.9 K. The more significant effect of the gas medium has been observed when changing rotation speed from 4π rad/s to 5π rad/s as in Figure 31. That is, CO_2 generates a lot larger difference value of ΔT_Y_{max} as 66.3 K than 12.2 K for N_2.

4.1.4 Measuring Acceleration and Rotation from Maximum Temperature Difference Values

Since the results in Figure 30 and Figure 31 are obtained only at 4π rad/s and 3*g*, respectively, to observe the consistency and reliability of results under varying conditions, we must also obtain these maximum temperature values at more wide ranges of rotational speeds and accelerations. These ΔT_X_{max} and ΔT_Y_{max} values around Heater 3 w.r.t acceleration (from 1*g* to 4*g*) and rotation (from 2π to 5π rad/s) using CO_2 as the gas medium are listed in Table 8 and Table 9, respectively. The *x*-sensor and *y*-sensor results with respect to changing acceleration and rotational speed are shown in Figure 32 and Figure 33, respectively.

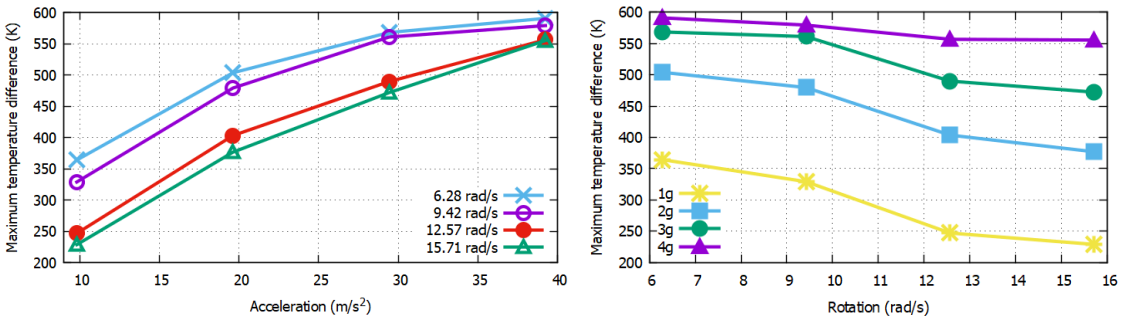

Figure 32- ΔT_{max} at X sensors w.r.t acceleration (a) and rotation (b) at varying rotation values by using CO_2 as the gas medium.

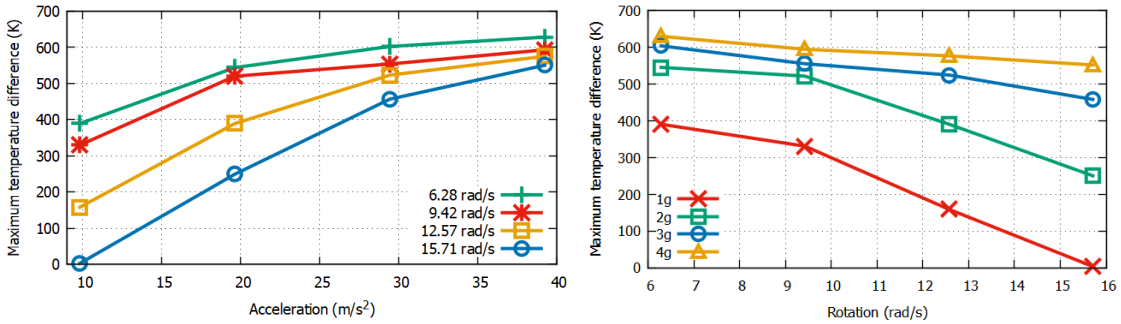

Figure 33- ΔT_{max} at Y sensors w.r.t acceleration (a) and rotation (b) at varying rotation values by using CO_2 as the gas medium.

Table 8- ΔT_X_{max} values around heater 3 (case 1).

		2π	3π	4π	5π
ΔT_X_{max} (K)	1*g*	364.3	329.2	247.0	228.9
	2*g*	503.9	479.5	403.5	377.0
	3*g*	568.4	561.1	489.9	472.2
	4*g*	591.0	579.4	556.7	555.4

Table 9- ΔT_Y_{max} values around heater 3 (case 1).

		2π	3π	4π	5π
ΔT_Y_{max} (K)	1*g*	389.7	330.2	238.6	225.4
	2*g*	544.4	520.5	389.8	345.0
	3*g*	602.8	554.3	523.5	457.1
	4*g*	628.6	593.4	575.6	550.7

It can be seen from Figure 32 and Figure 33 that sensitivity is higher at lower rotation speeds and higher accelerations. Conversely, resolution of the device is higher at higher rotation speeds and lower accelerations.

From Table 8 and Table 9, we can observe that the values of ΔT_X_{max} and ΔT_Y_{max} are both related to acceleration and rotation, which are to be measured by a real thermal motion sensor. Figure 34 shows three-dimensional plots of the values of ΔT_X_{max} and ΔT_Y_{max} produced by the accelerations (from 1*g* to 4*g*) and rotation (from 2π to 5π rad/s). The dots on both curves represent the data, extracted from Table 8 and Table 9, obtained by computational simulations. Due to the factor of cross-axis sensitivity, the acceleration applied in the *x*-direction and rotation around *z*-axis have generated temperature responses at *x*- and *y*-sensors. This is denoted by the relation:

$$\left(\Delta \mathrm{T}_x, \Delta \mathrm{T}_y\right) = f\left(a, \omega\right)$$

where ω is the rotational speed in rad/s and a is the acceleration.

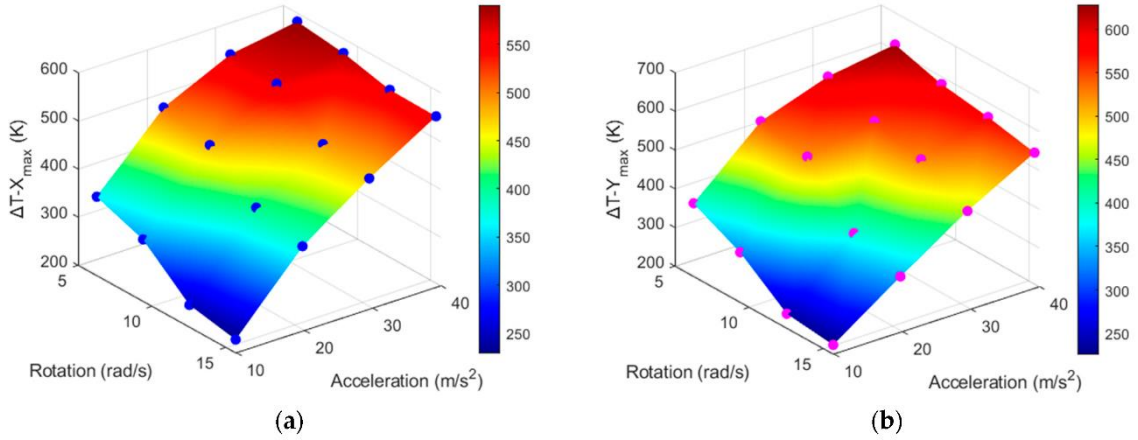

(a) (b)

Figure 34- ΔT_X$_{max}$ (a) and ΔT_Y$_{max}$ (b) produced with the given acceleration and rotation.

Since the temperature values obtained above are detected with the given acceleration and rotation values and change linearly, cubic interpolation using MATLAB has been employed to obtain more data. This is shown in Figure 35 and the data points are represented by the mesh points.

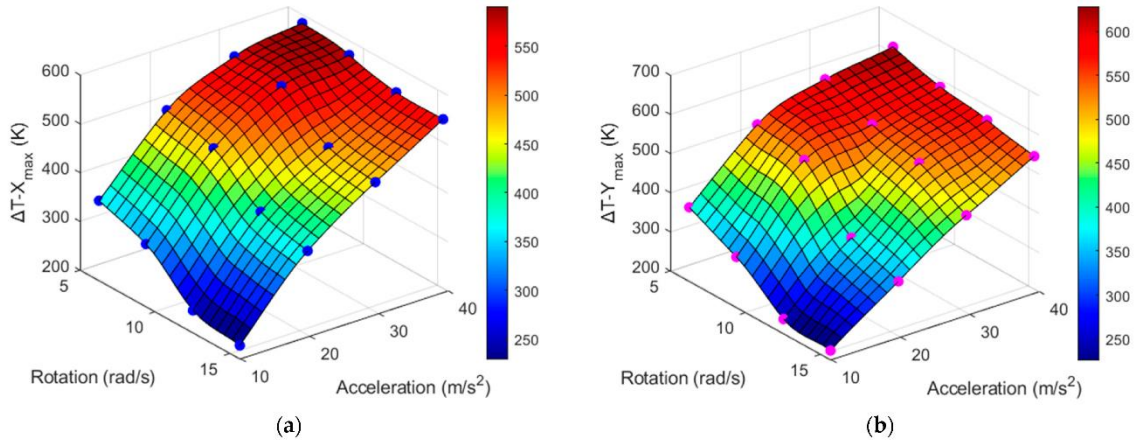

(a) (b)

Figure 35- Data obtained after interpolation of ΔT_X$_{max}$ (a) and ΔT_Y$_{max}$ (b) w.r.t acceleration and rotation.

Since the above temperature values, ΔT_X_{max} and ΔT_Y_{max} can be measured by the *x*- and *y*-sensors of the real thermal motion sensor, respectively, we need to obtain an inverse function such that the real thermal motion sensor can calculate a and ω corresponding to its measured maximum temperature difference (ΔT_{max}) values. This inverse function is represented in the equation below and the inverse graphs are shown in Figure 36, Figure 37, Figure 38 and Figure 39.

$$(a,\omega) = f^{-1}\left(\Delta \mathrm{T}_x, \Delta \mathrm{T}_y\right)$$

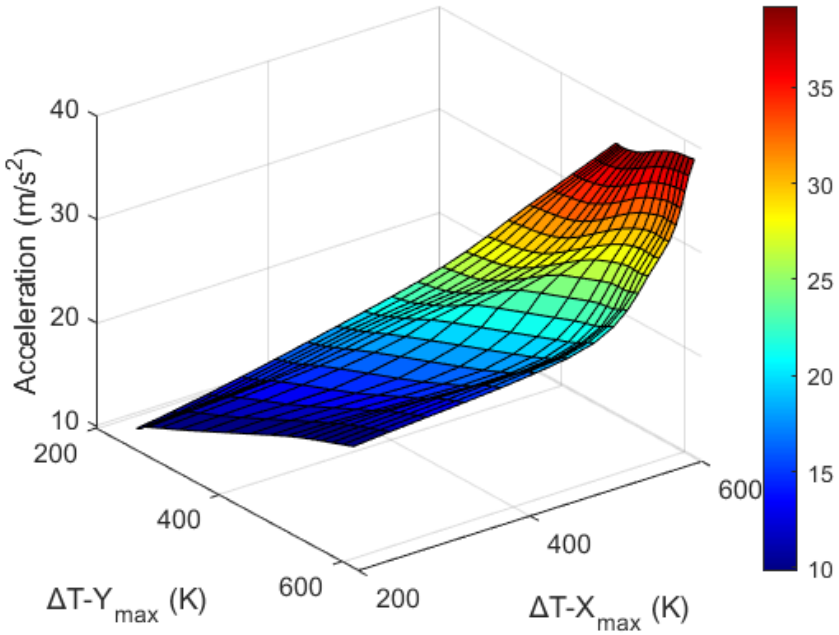

Figure 36- Graph to obtain a from ΔT_y and ΔT_x data measured around heater 3 (isometric drawing).

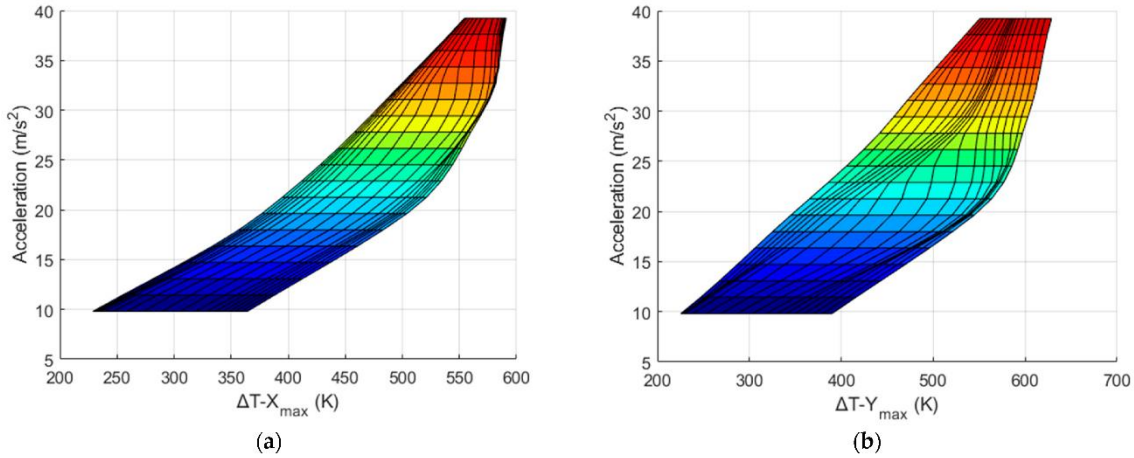

Figure 37- a w.r.t ΔT_x (a) and ΔT_y (b).

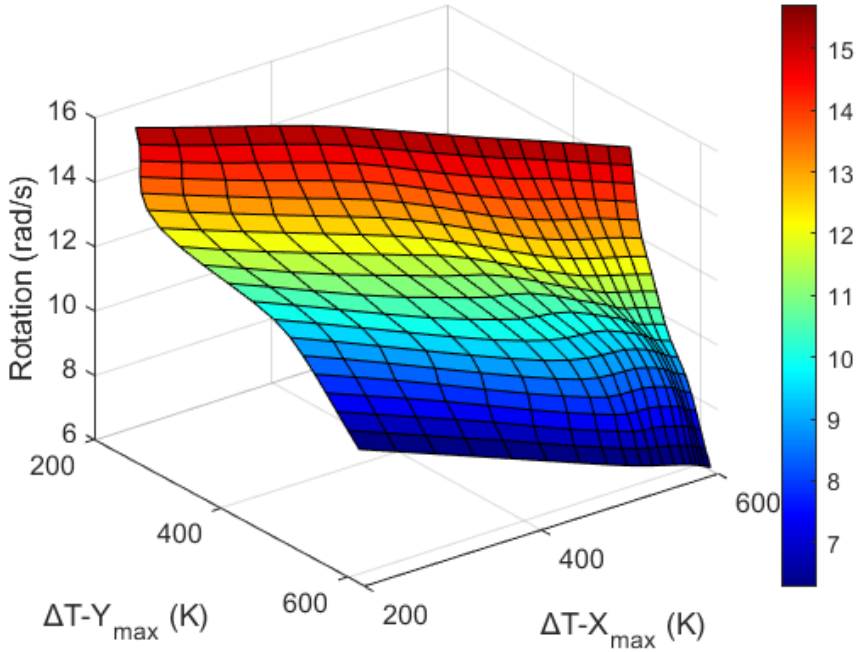

Figure 38- Graph to obtain ω from ΔT_y and ΔT_x data measured around heater 3 (isometric drawing).

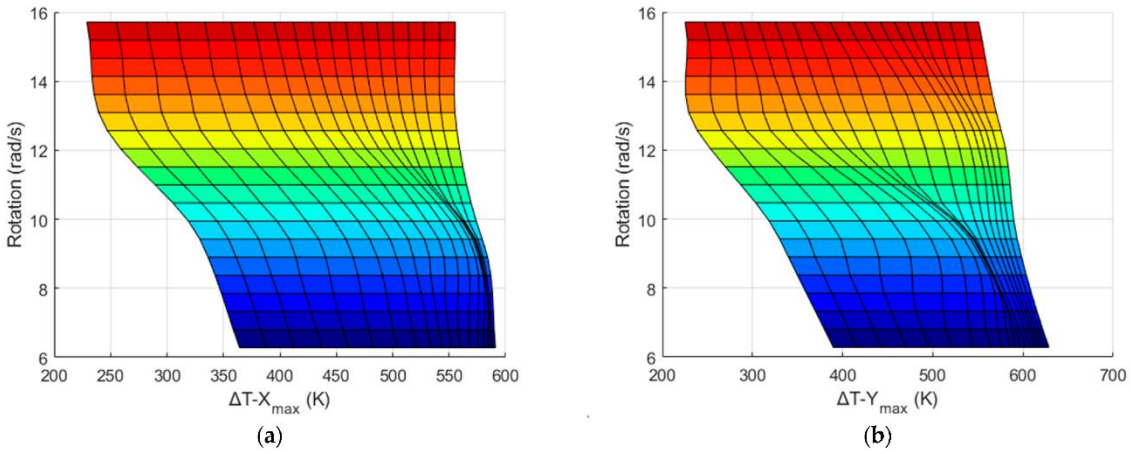

Figure 39- ω w.r.t ΔT_x (a) and ΔT_y (b).

For example, using the data shown in Figure 36 and Figure 37, the real thermal motion sensor can calculate the values of acceleration from the values of ΔT_y and ΔT_x measured by this sensor. To sum up, theoretically, from the results shown above, both rotation and the acceleration can be determined simultaneously when the real thermal motion sensor is rotating at any speed from 2π rad/s to 5π rad/s and accelerated in the *x*-direction at any value from 1*g* to 4*g*. This range of rotation speed and acceleration can be further increased when more simulations are conducted. In this case, the data is collected at *x*- and *y*-sensors around heater 3

only. Considering other heater positions with their four surrounding sensors should generate similar results.

4.2 Measuring X-acceleration and Z-amplitude of Vibrations

As described in section **4.1**, we have successfully demonstrated a technique by which X-acceleration and Z-rotation can be simultaneously measured. Moving forward, we have considered another scenario in which a body is accelerating in the *x*-direction and vibrating periodically along the *z*-axis. Therefore, X-acceleration and Z-amplitude of vibration are the two input physical quantities applied on a dual-axis thermal motion sensor. The computational model is the same as the one illustrated in Figure 11, the position of heaters and sensors is shown in Figure 13, and the mesh in Figure 16.

From Figure 13, any of the four heating sources along with their surrounding sensors can be considered for analysis. We have obtained the temperature response of the sensors around heater 1 i.e. ΔT_X_{max} and ΔT_Z_{max} as the two outputs which are defined by:

$$\Delta T\_X_{max} = T\_X11 - T\_X12$$

$$\Delta T\_Z_{max} = T\_Z11 - T\_Z12$$

Considering other heater positions with their four surrounding sensors should generate similar results as well. The next step is to calculate the maximum temperature difference value (ΔT_{max}) between a pair of equidistant sensors from the heaters. These are listed in Table 10 and Table 11 when acceleration in the x-direction (1*g*-4*g*) and vibration in the z-direction (0.03 m – 0.09 m amplitude) at 25 Hz frequency are applied simultaneously. The Z-maximum temperature difference (ΔT_Z_{max}) with respect to changing acceleration and amplitude are shown in Figure 40.

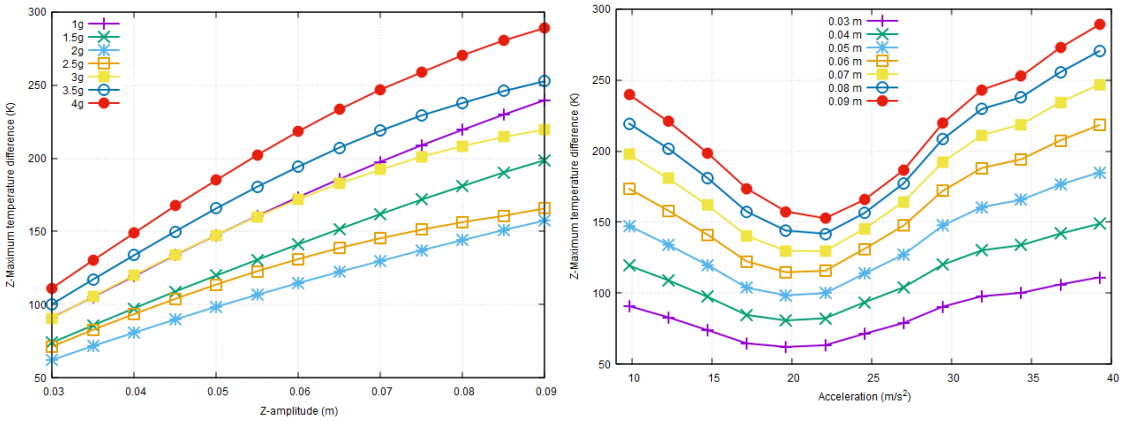

Figure 40- ΔT_Z_{max} w.r.t z-amplitude with varying acceleration (left) and x-acceleration at varying z-amplitudes (right).

Table 10- ΔT_X_{max} values around Heater 1 (case 2).

		0.03m	0.05m	0.07m	0.09m
ΔT_X_{max} (K)	1*g*	315.2	321.3	327.7	334.2
	2*g*	456.3	458.3	459.5	461.9
	3*g*	507.5	504.4	497.5	491.2
	4*g*	528.3	527.1	521.5	513.7

Table 11- ΔT_Z_{max} values around Heater 1 (case 2).

		0.03m	0.05m	0.07m	0.09m
ΔT_Z_{max} (K)	1*g*	92.1	151.9	203.4	244.1
	2*g*	59.7	94.1	124.6	151.8
	3*g*	86.8	142.1	186.1	213.4
	4*g*	114.5	189.6	251.8	294.4

From the data listed above, a surface graph is plotted in which maximum temperature difference values (ΔT_{max}) are listed with respect to acceleration and amplitude, as shown in Figure 41.

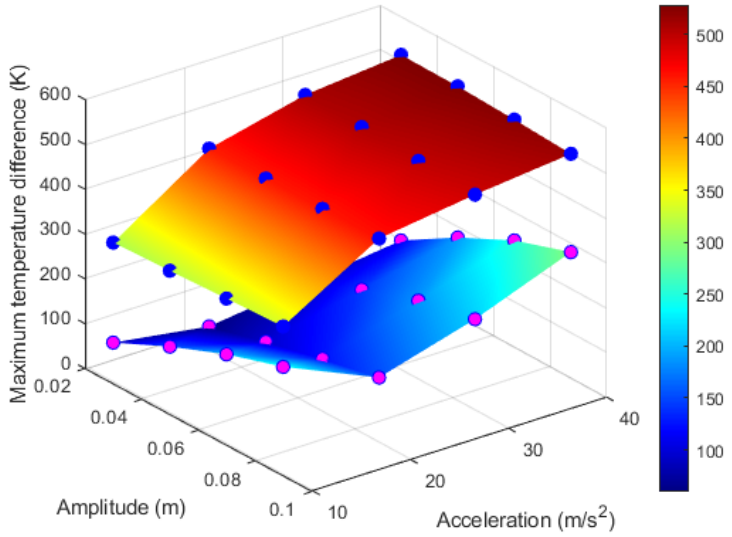

Figure 41- ΔT_X_{max} (blue dots) and ΔT_Z_{max} (purple dots) w.r.t given acceleration and amplitude of vibration.

Figure 41 shows the three-dimensional graph for Table 10 and Table 11. The blue dots on the graph surface represent ΔT_X_{max} and the purple dots show ΔT_Z_{max}. The problem is how to inversely obtain acceleration and amplitude from the data in Table 10 and Table 11 when ΔT_X_{max} and ΔT_Z_{max} are measured by the real sensor system. To do this, we need to obtain an inverse function. For this, however, more data is needed which is achieved by interpolating the data using the cubic interpolation technique in MATLAB and the surface is plotted in Figure 42.

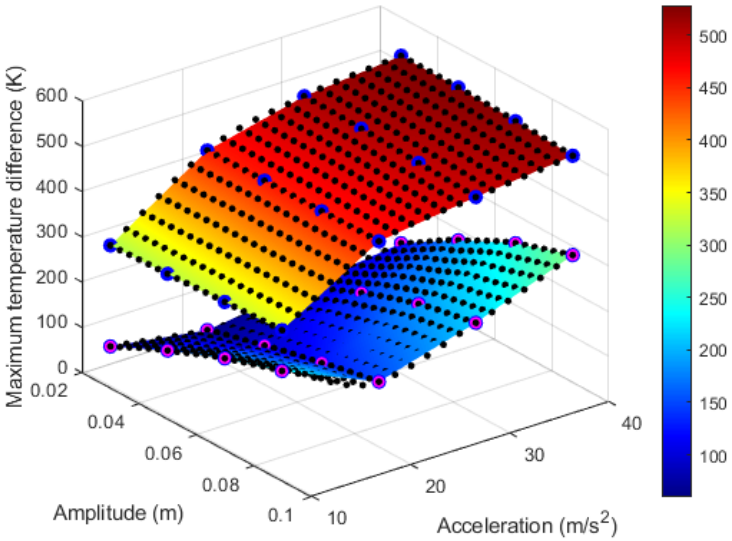

Figure 42- The data obtained from the interpolation (black bots) and the original data (the surface).

Figure 43 and Figure 44 illustrate the graphs that utilize the interpolated data from Figure 42. The *x*-axis represents ΔT_X_{max}, the y-axis represents ΔT_Z_{max}, and the *z*-axis represents X-acceleration and Z-amplitude, respectively.

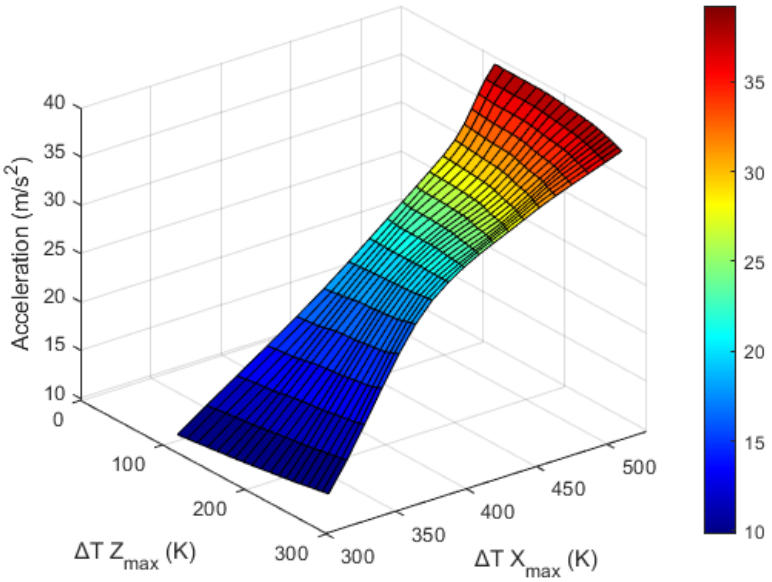

Figure 43- The graph to obtain x-acceleration from the data of ΔT_X_{max} and ΔT_Z_{max} (isometric drawing).

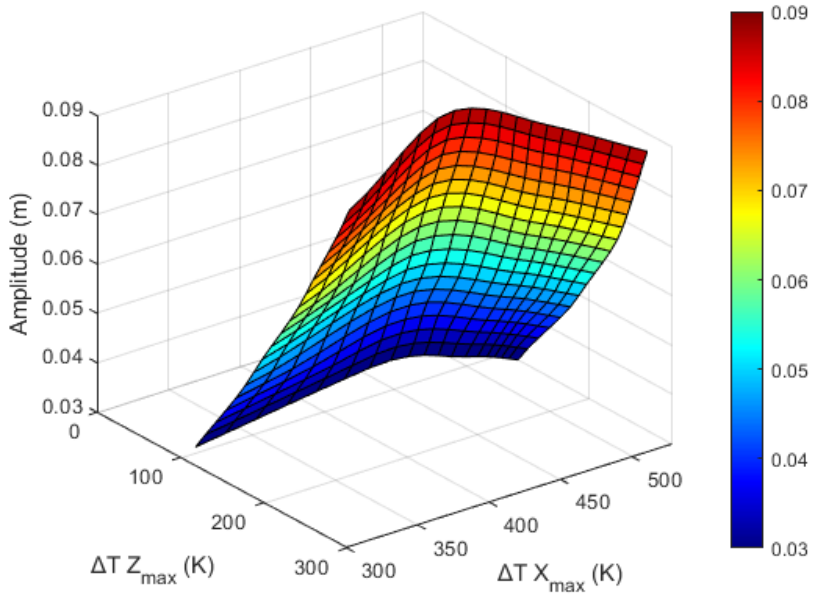

Figure 44- The graph to obtain z-amplitude from the data of ΔT_X_{max} and ΔT_Z_{max} (isometric drawing).

From the results shown above, both the acceleration and vibrational amplitude can be determined simultaneously when the real sensor system is accelerated in the *x*-direction at any

value from 1*g* to 4*g* and vibrated at the *z*-direction with amplitudes from 0.03 m to 0.09 m at 25 Hz frequency. The maximum acceleration and amplitude (4*g* and 0.09 m) can be increased if more simulations are conducted with larger values for acceleration and vibrational amplitudes.

From the temperature-time plots of the above data, an interesting pattern was observed. An example is illustrated in Figure 45, which is the graph at an X-acceleration of 2*g* and Z-vibration with an amplitude of 0.05 m at 25 Hz frequency.

The frequency of a wave is defined be to 2π/T, where T is the period. As the frequency of Z-vibration considered here is 25 Hz, this means a period of 0.2513 s. From Figure 45, it can be observed that the period of Z-vibration is approximately close to this value. Hence, we can say that the frequency of vibration, as a third physical quantity, can also be simultaneously measured by measuring the frequency of the temperature-time responses in addition to observing the data from the inverse functions.

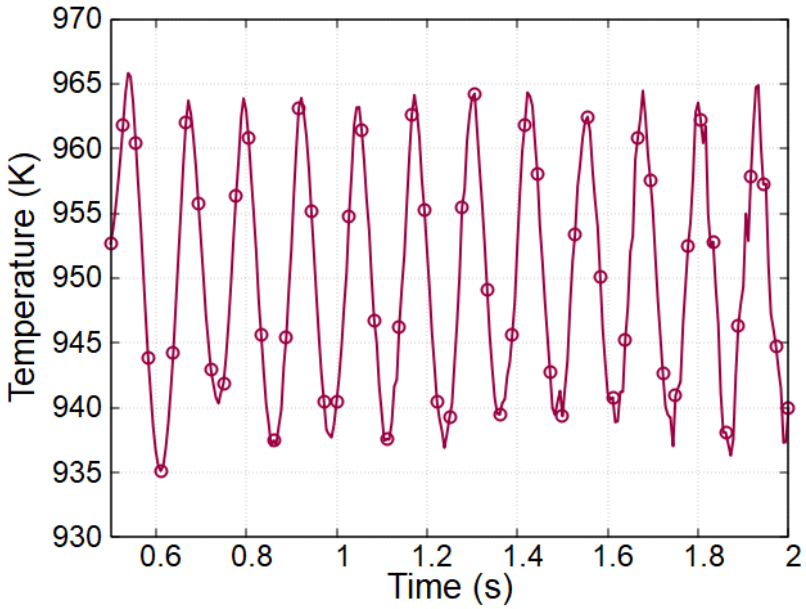

Figure 45- Temperature-time curve at 2g X-acceleration and Z-vibration at 0.05 m and 25 Hz.

Another observation, that can be made from Figure 43 and Figure 44 is that if a straight line is drawn parallel to the *z*-axis, no regions of multiple solutions are observed. This is probably because, when comparing vibration of a body and acceleration, it is imperative that both signals be measured on the same frequency range and with the same scale factors. Application of rotation along with acceleration, however, disrupts the frequency of the signal and hence non-uniformities in the trend are observed.

4.3 Measuring Acceleration and Rotation in All Three Directions

In sections **4.1** and **4.2**, we have shown the concept of measuring two quantities. The data extracted, however, is only for measuring X-acceleration and Z-rotation/amplitude of vibration. Due to the symmetry of the motion sensor, result is also valid for the acceleration applied in the *y*-direction along with the Z-rotation/amplitude of vibration. To further stretch on the results, in this section, we are proposing a method to obtain three inverse functions such that each inverse function measures one acceleration (a) and one rotation (ω) perpendicular to that acceleration. The inverse functions can be described as follows:

$$\left(a_x, \omega_z\right) = f^{-1}\left(\mathsf{T}_{x\max}, \mathsf{T}_{x\min}\right)$$

$$\left(a_y, \omega_x\right) = f^{-1}\left(\mathsf{T}_{y\max}, \mathsf{T}_{y\min}\right)$$

$$\left(a_z, \omega_y\right) = f^{-1}\left(\mathsf{T}_{z\max}, \mathsf{T}_{z\min}\right)$$

Cross-axis sensitivity (CAS) is to some extent present in all sorts of thermal sensors, including the one considered in this paper. In this case, by utilizing CAS, in order to simultaneously measure an acceleration and a rotation, we can extract peak temperature values (minimum and maximum) at the axis where only acceleration is applied. In section **4.1**, it was demonstrated that temperature data from both *x*- and *y*-axis can be utilized to simultaneously measure X-acceleration and Z-rotation. As a result, we can extract the data from the axis where only acceleration is applied by accounting for the influence of CAS.

The computational model and mesh for analysis are shown in Figure 14 and Figure 22, respectively. As indicated in Figure 9, temperature-time curves are generated via simulations using FLUENT software. To the cylindrical model, acceleration and rotation are simultaneously applied, and temperature graphs are analysed to extract the maximum and minimum values. To illustrate this process, Figure 46 shows the data acquired by the *Y12* sensor at a rotational velocity of 500°/s and 1–4*g* accelerations. The identified peak values are listed with respect to physical input quantities (Table 12, Table 13 and Table 14).

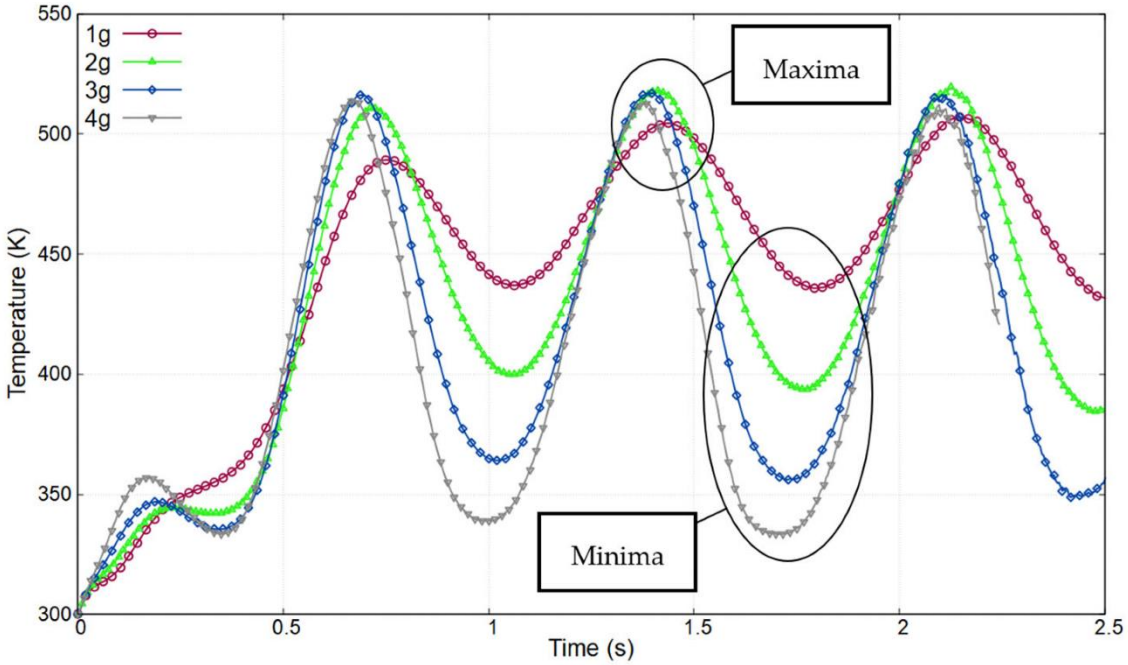

Figure 46- Temperature–time curve for Y12 sensor at 500°/s with varying accelerations from 1 to 4g.

Table 12- Data for T_X11_{max} and T_X11_{min} (case 3).

	a \ **ω**	**250**	**500**	**750**	**1000**
T_X11max	1 g	477.9	488.9	488.3	489.7
	2 g	495.0	502.6	501.1	500.7
	3 g	500.9	504.8	501.4	501.4
	4 g	498.4	503.3	495.5	496.7
	a \ **ω**	**250**	**500**	**750**	**1000**
T_X11min	1 g	407.1	415.7	417.3	415.7
	2 g	359.1	373.2	379.5	380.1
	3 g	328.3	338.5	346.1	348.9
	4 g	312.7	316.4	320.3	322.1

Table 13- Data for T_Y12_{max} and T_Y12_{min} (case 3).

	a \ ω	250	500	750	1000
T_Y12_{max}	1g	497.3	507.0	512.6	514.3
	2g	499.4	519.3	529.5	536.2
	3g	495.6	516.1	527.1	534.8
	4g	496.1	512.2	523.5	533.2
	a \ ω	**250**	**500**	**750**	**1000**
T_Y12_{min}	1g	425.9	435.8	440.6	440.0
	2g	381.3	393.7	404.0	408.1
	3g	353.7	355.9	361.3	361.0
	4g	337.6	333.4	332.3	329.3

Table 14- Data for T_YZ4_{max} and T_Z4_{min} (case 3).

	a \ ω	250	500	750	1000
T_Z4_{max}	1g	483.1	490.3	497.3	500.2
	2g	471.4	475.5	486.3	494.3
	3g	452.8	454.8	471.9	486.9
	4g	438.9	426.8	444.1	457.3
	a \ ω	**250**	**500**	**750**	**1000**
T_Z4_{min}	1g	442.4	440.6	438.4	444.8
	2g	388.2	398.6	401.7	399.7
	3g	350.7	354.8	360.0	360.2
	4g	332.2	329.4	333.2	334.0

This research study explores a range of accelerations from 1*g* to 4*g* (9.81 m/s^2 – 39.24 m/s^2) and rotations from 200°/s to 1000°/s in all three directions. As described in Figure 14, four heaters and pairs of temperature sensors are positioned in all three directions. Due to the symmetry of the structure, identical results are obtained at *X11* & *X21*, and *X12* & *X22*. Similarly, *Y11* & *Y21*, and *Z1* & *Z3* will provide similar extreme temperature values. Therefore, to obtain the extreme values, the maxima, and minima values of *X11*, *Y12*, and *Z4* are considered. These values are then recorded for all different accelerations and rotations in all three directions and correlated with the applied physical quantities of acceleration and rotation.

Since we have obtained results by computational simulation for only 4 data points for acceleration and rotation, we need to employ the interpolation technique to obtain more data between the upper and lower limits of input physical quantities. This is done in MATLAB using

the cubic interpolation technique that uses 4 data points to compute the polynomial. In this method, there are no constraints on the derivatives compared to other interpolation techniques such as spline interpolation.

The data for T_{max} and T_{min} values for all three axes are listed in Table 12, Table 13 and Table 14, and the inverse functions to obtain both acceleration and rotational speed in all three directions corresponding to the measured maximum and minimum temperature values are shown in Figure 47, Figure 48 and Figure 49. The node values indicate each data point. These inverse functions can then be installed in the computing unit of a real thermal motion sensor.

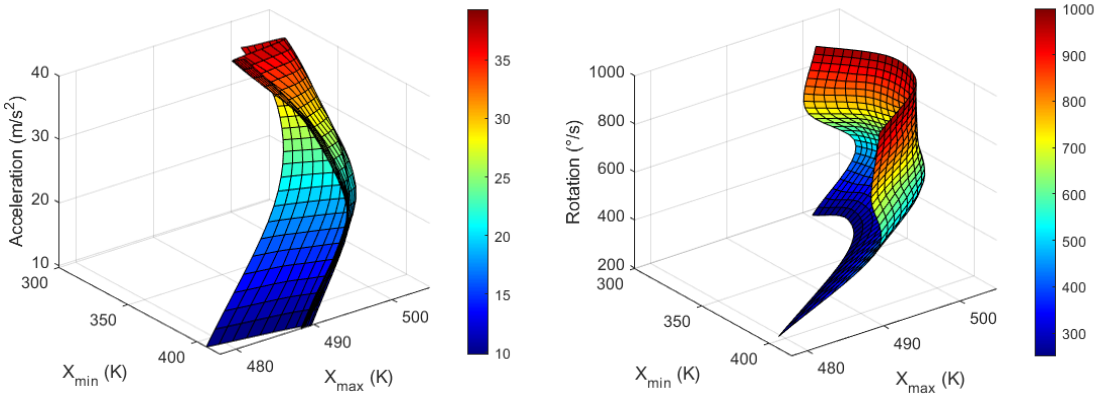

Figure 47- Graphs for X-acceleration (left) and Z-rotation (right) values from X_{min} and X_{max} measured around heater 1.

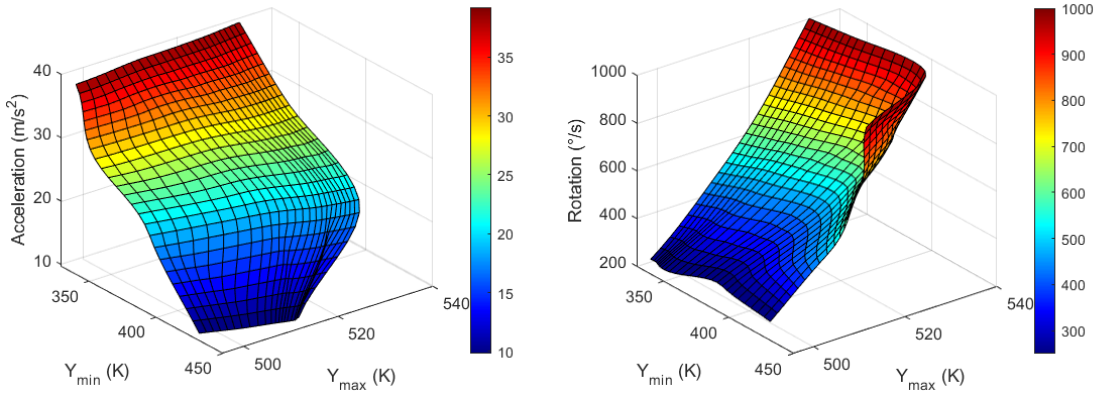

Figure 48- Graphs for Y-acceleration (left) and X-rotation (right) values from Y_{min} and Y_{max} measured around heater 2.

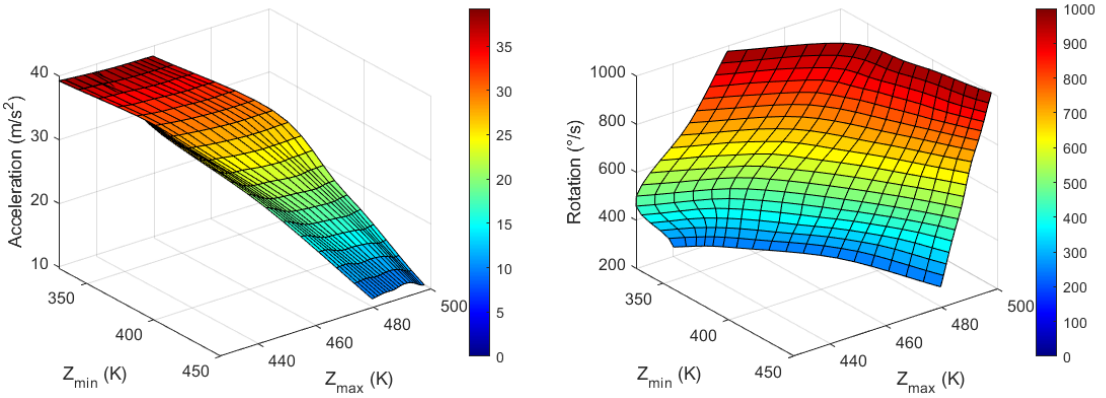

Figure 49- Graphs for Z-acceleration (left) and X-rotation (right) values from Z_{min} and Z_{max} measured around heater 4.

So, using the data from Figure 47, Figure 48 and Figure 49, a real thermal motion sensor can simultaneously measure all three accelerations at any value between 1 to 4*g* and rotation speeds between 200°/s –1000°/s. This range of acceleration and rotational speeds can be further increased when more simulations are conducted. Furthermore, more data should be extracted using simulations rather than relying on interpolation techniques to have more accurate results.

4.4 2D Mapping Method

To measure multiple physical quantities simultaneously, we have employed the methodology summarized in Figure 9. Similar technique was utilized to for all three cases, described in sections **4.1**, **4.2**, and **4.3**. For all these cases, an inverse function per physical quantity is essentially obtained and from that inverse function any value within the range can be measured corresponding to the output values (peak temperature values).

Here, we propose a mapping method (2D or 3D) that could be utilized to measure multiple physical quantities without using an inverse function. Taking into account case 3, Y-acceleration and X-rotation for the 2D method, input data, i.e., acceleration and rotational speeds, are plotted in a graph, as shown in the mapping of input data in Figure 50a (red lines). On the other hand, Figure 50b (red lines) shows the output data (T_{max} and T_{min}) extracted from Table 13. For actual measurements, once these 2D plots are obtained, for any output (measured) value of the sensor such as the purple circle in Figure 50b, the input value corresponding to the output value can be numerically and geometrically calculated (blue circle in Figure 50a) without needing an inverse function.

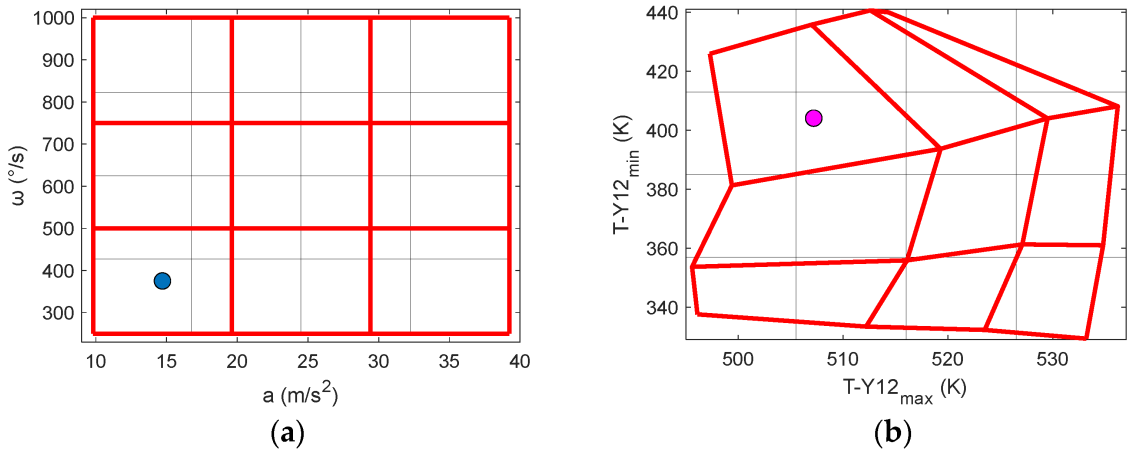

Figure 50- A 2D mapping of input data (a) and output data (b) extracted from Table 13.

It can be seen from Figure 50 that we can geometrically and numerically measure input physical quantities from the plot of output values. The 2D mapping technique shown above can be applied to the data of every sensor position. The plots for the data at *X11* and *Z4* are shown in Figure 51 and Figure 52, respectively.

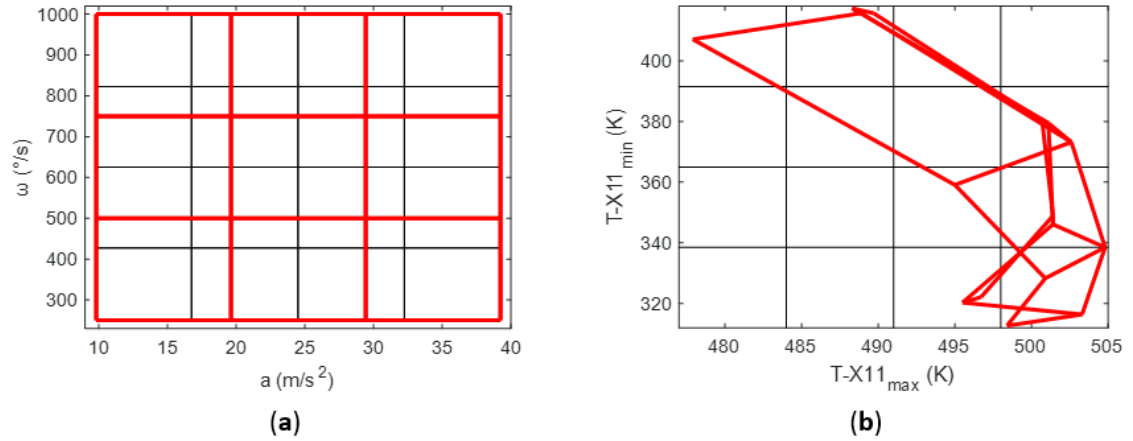

Figure 51- A 2D mapping of input data (a) and output data (b) extracted from Table 12.

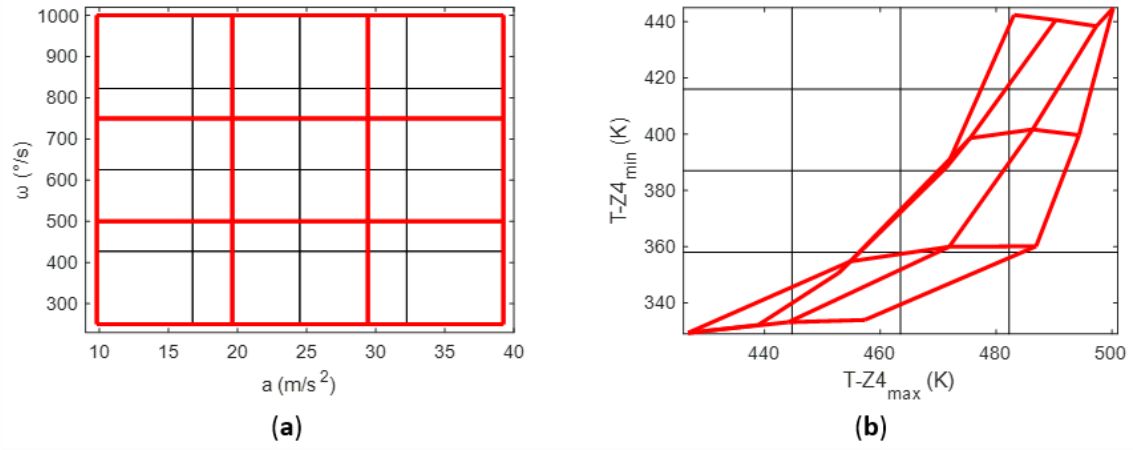

Figure 52- A 2D mapping of input data (a) and output data (b) extracted from Table 14.

It can be observed from Figure 51 that some of the quadrilateral shapes overlap with each other for the output data, this indicates regions of multiple solutions. This method is also efficient in determining the areas of multiple solution as compared to the inverse function method, as it can be easily visualized with the 2D plots.

This novel method can also be applied in 3D to achieve measurement of three physical quantities simultaneously. These are demonstrated in Figure 53 and Figure 54.

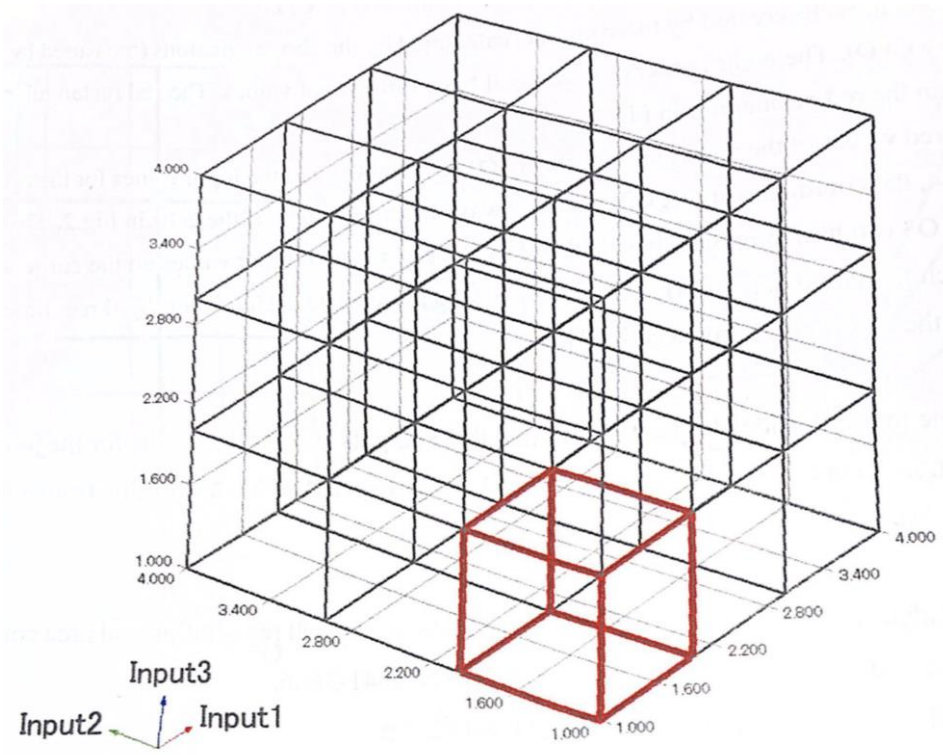

Figure 53- Cells of three inputs

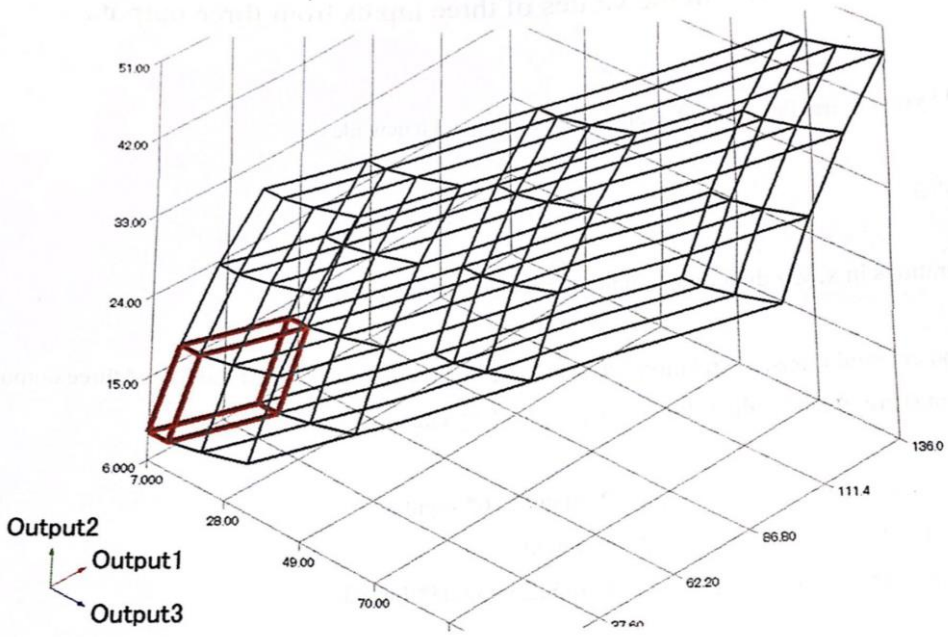

Figure 54- Cells of three outputs

Figure 53 shows the cells created by three inputs with each input positioned in *x*-, *y*-, and *z*-axis. The eight corners of each cell are supposed to have three outputs that are either

measured by the real sensor or simulated by CFD. A mathematical equation can be established for each output value with respect to the input values. Figure 54 shows the cells created by three outputs which would be calculated by the mathematical equation. The eight corners of each have three corresponding input values. The red rectangular prism in Figure 53 is transformed into the red octahedron in Figure 54.

For all the values that lie within the range of the graph demonstrated in Figure 53 and Figure 54, the coordinate of *Output1*, *Output2*, and *Output3* always belongs to the one of the cells in Figure 53. Then the input values for these outputs can be approximately calculated by the eight sets of input values on the corners of this cell.

Different numerical approaches can be utilized to find this. The cell in which the coordinate of the outputs values belongs to can be found by three-dimensional approaches developed from the algorithms as introduced by Ogami [78]. The paper presented some effective computational methods for particle searching and positioning by 'cell registration' and 'area comparison' methods. Both these methods are applicable to structured and unstructured grid systems.

Chapter 5: Discussion

In this study, we have presented a novel technique that can be implemented to measure multiple physical quantities simultaneously using a thermal motion sensor. We have successfully implemented and demonstrated the simultaneous application of acceleration and rotation (section **4.1**), acceleration and amplitude of vibration (section **4.2**), and acceleration and rotation in all three directions (section **4.3**).

A general method can be mentioned here. The idea is to define a relationship between multiple physical quantities that we are interested in, and multiple outputs by computational simulations as generalized below:

(output 1, output 2, …) = f (physical quantity 1, physical quantity 2, …)

For each value of a physical quantity, there is a corresponding set of outputs (ΔT_{max} and T_{max} values in our case). Number of outputs, however, should be the same as the number of input physical quantities. That is why cross-axis sensitivity is useful. Once this relation has been obtained, the next step is to find the inverse function of this relationship as:

(physical quantity 1, physical quantity 2, …) = f^{-1} (output 1, output 2, …)

Using this relation, we can easily obtain a graphical inverse function with a specific range of physical quantities. Within that range, any value can be extracted concerning its output. In this study, for case 1, the maximum temperature values ΔT_{max} around the *X* and *Y* sensors were obtained as two outputs corresponding to acceleration in the *x*-direction and rotation around the *z*-axis. For case 2, the maximum temperature values ΔT_{max} around the *x*- and *z*-sensors were accounted for as the two outputs corresponding to x-acceleration and amplitude of vibration applied to the *z*-axis. For case 3, however, six inverse functions were obtained and T_{max} and T_{min} values were taken as the outputs. Each inverse function measured one acceleration and a rotation perpendicular to the axis where acceleration was applied. These data of the inverse function can then be installed in the computing unit of a real thermal motion sensor so that the sensor can calculate the input physical quantities from the measured output values.

If the size of the aerial system is increased while keeping the heater power of the thermal motion sensor constant, similar graph trends as well as performance parameters like sensitivity should be generated. As described in section **2.6**, sensitivity of a thermal accelerometer can be represented by the Grashof number, and in fluid mechanics, numbers such as Reynold's number

and Prandtl number are considered dimensionless groups and therefore the trends remain similar. So, if the size of the aerial system is changed, the temperature values and inverse functions need not be altered. It is dependent on the input physical quantities. Moreover, the acceleration and rotation/amplitude of vibration range considered here is limited and should be further extended to practically account for any value applied to the device. Once more data is obtained by computational simulations, in order to incorporate a broader range, the thermal motion sensor's computing unit can be enhanced by integrating the modified inverse function.

According to Nguyen [79] and Ogami [6], when working with a 3-axis thermal accelerometer, they have discussed the idea of cross-axis sensitivity as "the same response can be observed for two accelerations with different magnitudes and opposite signs" which means that two combinations of temperature outputs determined a single acceleration. In section **4.1**, we had acceleration in the *x*-direction and rotation around the *z*-direction but even by considering X and Y-sensor responses, because of cross-axis sensitivity, results were observed to have a unique combination of temperature outputs corresponding to accelerations of 1*g*-4*g* and rotational speeds 2π -5π rad/s. We have defined such a characteristic of results as the *uniqueness* of the solution. For 0.1254 cm and 0.1433 cm distances between heater and sensors, we observed areas of multiple solutions for changing rotational speeds. Therefore, for a defined range of input physical quantities, we need to verify the results by simulations and find such parameters that generate unique solutions.

In section **4.1.2**, we observed that the shorter the distance between the heater and sensors is, the better sensitivity and resolution are observed. Six different positions of sensors were considered, amongst which the shortest distance, 0.0179 cm, gave the most favourable results while the largest one, 0.1433 cm, was the least. This means that reducing this distance to the least possible value would generate better performance for the device. However, this distance is measured from the center of the heater to the center of sensors, so considering the practical aspects there is a limit to how much this can be decreased. Therefore, a compromise is needed in choosing the ideal distance between the heater and sensors.

In addition to sensitivity and resolution, another important factor that determines the quality of results is the frequency response. It is a measure of how quickly the device can respond to changes in acceleration and rotation speeds. To obtain a fast and wider frequency response, we need to change the thermal physical properties of the gas medium. A large thermal

conductivity (α) and a small density (ρ) will accelerate the thermal diffusion, which consequently facilitates the heat balance in the cavity and provide fast frequency response to the device. Multiple works in literature have studied the frequency response of a thermal accelerometer. Garraud [80] investigated the frequency response using an analytical and CFD model. This could also be done for a thermal motion sensor measuring multiple physical quantities, which can be an interesting study as a future work.

For our thermal motion sensor's material, we have used polyvinylidene fluoride (PVDF), which is also known for its piezoelectric behaviour. This means that it can generate an electric charge in response to applied mechanical stress. Therefore, by using this to our advantage, we may also define a new variable concerning pressure changes around the body. By using this application of the material, we can measure one additional physical quantity such as applied mechanical stress simultaneously. PVDF, however, has a high value of the coefficient of thermal expansion (α) which limits its usage at higher values of temperature. The properties and responsiveness of PVDF concerning a thermal motion sensor for measuring pressure can be investigated as a future work.

One problem encountered in the inverse functions is the region of multiple solutions. This is the region where two identical combinations of maximum and minimum temperature values generate different input physical quantities. This would render an inaccurate result. This region can be viewed by drawing a vertical line from the XY plane parallel to the input physical quantity axis. For measuring Y-acceleration using T_Y_{max} and T_Y_{min}, this region is demonstrated by an eclipse in Figure 55. Therefore, it is necessary to verify the results and find parameters that generate unique solutions. This may be reduced by either altering the cavity shape of the sensor or changing the position of heaters and sensors.

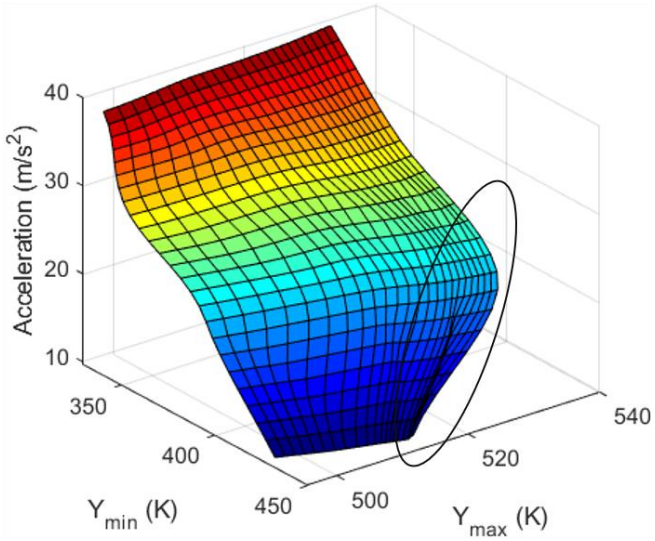

Figure 55- Region of multiple solutions indicated on the graph to obtain Y-acceleration using Y_{max} and Y_{min}.

As no experimental or theoretical model is presented in this paper to support or validate the numerical simulations. Our future work will be manufacturing a real thermal device using the results presented in this paper. However, the technique presented in this study may provide a cost-effective and time-saving solution to the sensor technology of UAVs.

In case 3 (section **4.3**), for measuring acceleration and rotation in all three directions, the method has the disadvantage of requiring both acceleration and rotation. However, by examining both rotary-wing and fixed-wing UAVs it can be observed that the pitch motion along the transverse or lateral axis is a vital factor in facilitating smooth and efficient flight throughout the entire operational duration of the device. Furthermore, a study should also be explored in which more than two quantities can be measured using a single inverse function must be conducted. The idea for this was proposed in section **4.4** in which 3D mapping can be utilized for obtaining three outputs to measure three physical quantities simultaneously.

Chapter 6: Conclusion

In this study, by using the concept of computational fluid dynamics (CFD) and leveraging cross-axis sensitivity (CAS) in thermal accelerometers, we have presented a novel technique for measuring multiple physical quantities simultaneously. As observed in section **4.1**, for any acceleration between 9.81 m/s^2 and 39.24 m/s^2 (1*g*–4*g*) and rotational speed of 6.28 rad/s–15.71 rad/s, this device is capable of measuring both quantities simultaneously. The range of acceleration and rotation can be further expanded by additional computational simulations. The inverse function can then be installed in the computing unit of a real thermal motion sensor so that the sensor can calculate the acceleration and rotation speed from the measured temperature values.

In sections **4.1.2** and **4.1.3**, a parametric study was conducted where two parameters were investigated and by altering those parameters, the performance of the device was evaluated. It was concluded that the sensitivity and resolution of the device may be increased by considering a lower distance between heater and sensors, although a compromise is needed such that there is a sufficient distance between heater and sensors. 0.0537 cm was considered to be a good distance for the MEMS thermal motion sensor. Furthermore, by utilizing a gas medium with a high density and a low viscosity such as CO_2 may also improve the sensitivity and resolution.

In section **4.2**, we have shown that any acceleration between 9.81 m/s^2 and 39.24 m/s^2 (1*g*–4*g*) and amplitude of vibration of 0.03 m – 0.09 m at 25 Hz along the z-axis can also be measured simultaneously using the inverse function approach. It was also observed that the frequency of the temperature response was identical to the frequency of vibration. This indicates that the frequency of vibration can be the third quantity which can be measured simultaneously.

In section **4.3**, further extending the idea of measuring two quantities, we have proposed a concept by which acceleration and rotation can be measured simultaneously in all three directions, *x*–, *y*– and *z*–axis for applications in unmanned aerial vehicles (UAVs). This is again achieved by utilizing CAS. For X-acceleration and Z-rotation, we have extracted maxima and minima of the temperature-time curves of the X-sensor data. Similarly, for Y-acceleration and X-rotation, the data from Y-sensor were considered, and Z-sensor data for Z-acceleration and Y-rotation. In this way we have obtained six graphical plots, one for each acceleration and rotation, such that any acceleration from 1 to 4*g* and rotation from 200 to 1000°/s can be measured

simultaneously. Once obtained by computational simulations, these inverse function plots can then be integrated into the computing unit a real thermal motion sensor.

In section **4.4** we introduced a novel approach known as 2D or 3D mapping, which allows us to accurately measure multiple physical quantities by analysing the plotted output values in relation their corresponding input values. This technique offers an efficient numerical measurement, and this may be a better approach than using inverse function, as the values can be measured numerically and geometrically.

In all four subsections of **Chapter 4** we have introduced a concept by which modifying a thermal motion sensor and leveraging CAS, we were able to measure multiple physical quantities simultaneously. In this study, we obtained output values by observing temperature data, however we believe that by quantifying other quantities such as pressure, this idea can also be applicable to other sensor types such stress sensors or vibration sensors. Additionally, a frequency response analysis and an effective sensitivity analysis is missing in this study which should be thoroughly conducted to verify the quality of the results.

The results obtained by CFD simulations here needs to be tested and validated either through theoretical analysis or real-world experiments using the MEMS manufacturing technology. However, overall, this methodology provides a strong framework for measuring multiple physical quantities and allows researchers all over the world to gain deeper insights into this new concept and obtain experimental data. This study offers an excellent solution to the challenges faced by sensor technology in UAVs.

Bibliography

[1] B. Brzozowski, Z. Rochala, and K. Wojtowicz, “Overview of the research on state-of-the-art measurement sensors for UAV navigation,” in *4th IEEE International Workshop on Metrology for AeroSpace*, Padua, Italy, 2017, pp. 565–570.

[2] I. A. Faisal, T. W. Purboyo, A. Siswo, and R. Ansori, “A Review of Accelerometer Sensor and Gyroscope Sensor in IMU Sensors on Motion Capture,” 2020.

[3] S. J. Chen and C. S. Shen, “A novel two-axis CMOS accelerometer based on thermal convection,” *IEEE Trans Instrum Meas*, vol. 57, no. 8, pp. 1572–1577, Aug. 2008, doi: 10.1109/TIM.2008.925347.

[4] K. Siddique and Y. Ogami, “Computational Study on Thermal Motion Sensors That Can Measure Acceleration and Rotation Simultaneously,” *Sensors*, vol. 22, no. 18, 2022, doi: 10.3390/s22186744.

[5] K. Siddique and Y. Ogami, “Computational Study of a Motion Sensor to Simultaneously Measure Two Physical Quantities in All Three Directions for a UAV,” *Sensors*, vol. 23, no. 11, p. 5265, Jun. 2023, doi: 10.3390/s23115265.

[6] Y. Ogami, N. Murakita, and K. Fukudome, “Computational experiments on the step and frequency responses of a three-axis thermal accelerometer,” *Sensors (Switzerland)*, vol. 17, no. 11, Nov. 2017, doi: 10.3390/s17112618.

[7] M. H. Zawawi *et al.*, “A review: Fundamentals of computational fluid dynamics (CFD),” in *AIP Conference Proceedings*, American Institute of Physics Inc., Nov. 2018. doi: 10.1063/1.5066893.

[8] “ CFD-ACE+ (ESI-Group). CFD-ACE+ (ESI-Group),” 2004.

[9] “ CFX,” 2004.

[10] “Flow-3D (Flow Science, Inc),” 2008. [Online]. Available: www.flow3d.com!

[11] “Fluent Inc., Fluent (Fluent Inc.),” 2003.

[12] T. Glatzel *et al.*, “Computational fluid dynamics (CFD) software tools for microfluidic applications - A case study,” *Comput Fluids*, vol. 37, no. 3, pp. 218–235, Mar. 2008, doi: 10.1016/j.compfluid.2007.07.014.

[13] “FLUENT 6.1 UDF Manual,” 2003.

[14] B. Foluso Ladeinde, M. Ashrae, and M. D. Nearon, “CFD Applications In the HVAC&R Industry,” *ASHRAE J*, vol. 39, pp. 44–48, 1997.

[15] B. Xia and D. W. Sun, “Applications of computational fluid dynamics (cfd) in the food industry: a review,” *Comput Electron Agric*, vol. 34, no. 1–3, pp. 5–24, May 2002, doi: 10.1016/S0168-1699(01)00177-6.

[16] A. Jameson and J. Vassberg, “Computational fluid dynamics for aerodynamic design - Its current and future impact,” in *39th Aerospace Sciences Meeting and Exhibit*, Reston,

Virigina: American Institute of Aeronautics and Astronautics, Jan. 2001. doi: 10.2514/6.2001-538.

[17] P. Iob, L. Frau, P. Danieli, L. Olivieri, and Bettanini Carlo, “Avalanche Rescue with Autonomous Drones,” in *IEEE 7th International Workshop on Metrology for AeroSpace (MetroAeroSpace)*, 2020, pp. 319–324.

[18] H. Nawaz, H. M. Ali, and S.-R. Massan, “Applications of unmanned aerial vehicles: a review,” *3C Tecnología_Glosas de innovación aplicadas a la pyme*, pp. 85–105, Nov. 2019, doi: 10.17993/3ctecno.2019.specialissue3.85-105.

[19] S. Yaprak, Ö. Yildirim, and T. Susam, “UAV Based Agricultural Planning and Landslide Monitoring,” *TeMA Journal of Land Use Mobility and Environment*, vol. 3, pp. 325–338, 2017, [Online]. Available: www.tema.unina.it

[20] P. K. Reddy Maddikunta *et al.*, “Unmanned Aerial Vehicles in Smart Agriculture: Applications, Requirements, and Challenges,” *IEEE Sens J*, vol. 21, no. 16, pp. 17608–17619, Aug. 2021, doi: 10.1109/JSEN.2021.3049471.

[21] Amazon Staff, “Amazon Prime Air prepares for drone deliveries,” Jun. 2022. Accessed: Jun. 02, 2023. [Online]. Available: https://www.aboutamazon.com/news/transportation/amazon-prime-air-prepares-for-drone-deliveries

[22] A. N. Wilson, A. Kumar, A. Jha, and L. R. Cenkeramaddi, “Embedded Sensors, Communication Technologies, Computing Platforms and Machine Learning for UAVs: A Review,” *IEEE Sensors Journal*, vol. 22, no. 3. Institute of Electrical and Electronics Engineers Inc., pp. 1807–1826, Feb. 01, 2022. doi: 10.1109/JSEN.2021.3139124.

[23] E. Ebeid, M. Skriver, K. H. Terkildsen, K. Jensen, and U. P. Schultz, “A survey of Open-Source UAV flight controllers and flight simulators,” *Microprocess Microsyst*, vol. 61, pp. 11–20, Sep. 2018, doi: 10.1016/J.MICPRO.2018.05.002.

[24] L. Reddy Cenkeramaddi, J. Bhatia, A. Jha, S. Kumar Vishkarma, and J. Soumya, “A Survey on Sensors for Autonomous Systems,” in *2020 15th IEEE Conference on Industrial Electronics and Applications (ICIEA)*, IEEE, Nov. 2020, pp. 1182–1187. doi: 10.1109/ICIEA48937.2020.9248282.

[25] J. Svensgaard, S. M. Jensen, S. Christensen, and J. Rasmussen, “The importance of spectral correction of UAV-based phenotyping with RGB cameras,” *Field Crops Res*, vol. 269, p. 108177, Jul. 2021, doi: 10.1016/J.FCR.2021.108177.

[26] X. Dai, Y. Mao, T. Huang, B. Li, and D. Huang, “Navigation of Simultaneous Localization and Mapping by Fusing RGB-D Camera and IMU on UAV,” in *2019 CAA Symposium on Fault Detection, Supervision and Safety for Technical Processes (SAFEPROCESS)*, IEEE, Jul. 2019, pp. 6–11. doi: 10.1109/SAFEPROCESS45799.2019.9213339.

[27] H. Kayan, R. Eslampanah, F. Yeganli, and M. Askar, “Heat leakage detection and surveiallance using aerial thermography drone,” in *2018 26th Signal Processing and*

Communications Applications Conference (SIU), IEEE, May 2018, pp. 1–4. doi: 10.1109/SIU.2018.8404366.

[28] C. Eling, L. Klingbeil, and H. Kuhlmann, “Real-Time Single-Frequency GPS/MEMS-IMU Attitude Determination of Lightweight UAVs,” *Sensors*, vol. 15, no. 10, pp. 26212–26235, Oct. 2015, doi: 10.3390/s151026212.

[29] C. Vincenzo Angelino, V. Rosario Baraniello, and L. Cicala, “High altitude UAV navigation using IMU, GPS and camera,” in *16th International Conference on Information Fusion*, 2013, pp. 647–654.

[30] D. G. Davies, R. C. Bolam, Y. Vagapov, and P. Excell, “Ultrasonic sensor for UAV flight navigation,” in *2018 25th International Workshop on Electric Drives: Optimization in Control of Electric Drives (IWED)*, IEEE, Jan. 2018, pp. 1–7. doi: 10.1109/IWED.2018.8321389.

[31] S. Rahman and D. A. Robertson, “Radar micro-Doppler signatures of drones and birds at K-band and W-band,” *Sci Rep*, vol. 8, no. 1, Dec. 2018, doi: 10.1038/s41598-018-35880-9.

[32] G. Greco, C. Lucianaz, S. Bertoldo, and M. Allegretti, “A solution for monitoring operations in harsh environment: A RFID reader for small UAV,” in *2015 International Conference on Electromagnetics in Advanced Applications (ICEAA)*, IEEE, Sep. 2015, pp. 859–862. doi: 10.1109/ICEAA.2015.7297235.

[33] A. Digulescu, C. Despina-Stoian, F. Popescu, D. Stanescu, D. Nastasiu, and D. Sburlan, “UWB Sensing for UAV and Human Comparative Movement Characterization,” *Sensors*, vol. 23, no. 4, p. 1956, Feb. 2023, doi: 10.3390/s23041956.

[34] W. Wang, T. Zhang, D. Fan, and C. Xing, “Study on frequency stability of a linear-vibration mems gyroscope,” *Microsystem Technologies*, vol. 20, no. 12, pp. 2147–2155, Sep. 2014, doi: 10.1007/s00542-013-1951-4.

[35] H. Chang, X. Gong, S. Wang, P. Zhou, and W. Yuan, “On improving the performance of a triaxis vortex convective gyroscope through suspended silicon thermistors,” *IEEE Sens J*, vol. 15, no. 2, pp. 946–955, Feb. 2015, doi: 10.1109/JSEN.2014.2358700.

[36] D. Bremner, “THE IMPORTANCE OF SENSORS TO THE INTERNET OF THINGS,” 2015. [Online]. Available: http://eprints.gla.ac.uk/105145/http://eprints.gla.ac.uk

[37] M. K. Mishra, V. Dubey, P. M. Mishra, and I. Khan, “MEMS Technology: A Review,” *Journal of Engineering Research and Reports*, pp. 1–24, Feb. 2019, doi: 10.9734/jerr/2019/v4i116891.

[38] T. S. Fanse, “Micro-Electro-Mechanical System (MEMS) Application and Prospects in Automobile,” *IOSR Journal of Mechanical and Civil Engineering (IOSR-JMCE) e-ISSN*, vol. 19, pp. 17–21, doi: 10.9790/1684-1901021721.

[39] A. Wung, R.V. Park, K.J. Rebello, and G.K. Fedder, “Tri-axial high-g CMOS-MEMS capacitive accelerometer array,” in *21st International Conference on Micro Electro Mechanical Systems*, Tucson, AZ, USA, 2008.

[40] T. K. , R. A. L. Bhattacharyya, “Micro and Smart Devices and Systems,” in *Micro and Smart Devices and Systems. Springer Tracts in Mechanical Engineering*, 2014, pp. 19–34.

[41] N. Yazdi, F. Ayazi, and K. Najafi, “Micromachined Inertial Sensors,” 1998.

[42] Y. Ning, Y. Loke, and G. McKinnon, “Fabrication and characterization of high g-force, silicon piezoresistive accelerometers,” *Sens Actuators A Phys*, vol. 48, no. 1, pp. 55–61, 1995.

[43] L. Liu, H. Zhou, W. Li, and H. Guo, “Structure design and optimization of high-g piezoresistive accelerometer,” in *Proceedings of 2011 International Conference on Electronic & Mechanical Engineering and Information Technology*, IEEE, Aug. 2011, pp. 4508–4511. doi: 10.1109/EMEIT.2011.6024031.

[44] “Piezoelectric Accelerometers Theory and Application,” 2001. Accessed: Jun. 01, 2023. [Online]. Available: https://www.gracey.co.uk/downloads/accelerometers.pdf

[45] M. Varanis, A. Silva, A. Mereles, and R. Pederiva, “MEMS accelerometers for mechanical vibrations analysis: a comprehensive review with applications,” *Journal of the Brazilian Society of Mechanical Sciences and Engineering*, vol. 40, no. 11, Nov. 2018, doi: 10.1007/s40430-018-1445-5.

[46] S Tadigadapa and K Mateti, “Piezoelectric MEMS sensors: state-of-the-art and perspectives,” *Meas Sci Technol*, vol. 20, no. 9, 2009, doi: 10.1088/0957-0233/20/9/092001.

[47] S. R. Anton and H. A. Sodano, “A review of power harvesting using piezoelectric materials (2003–2006),” *Smart Mater Struct*, vol. 16, no. 3, pp. R1–R21, Jun. 2007, doi: 10.1088/0964-1726/16/3/R01.

[48] S. Elies, “Performance Analysis of Commercial Accelerometers: A Parameter Review,” *Sensors & Transducers*, vol. 193, pp. 179–190, 2015, [Online]. Available: http://www.sensorsportal.com

[49] X. Jiang, K. Kim, S. Zhang, J. Johnson, and G. Salazar, “High-temperature piezoelectric sensing,” *Sensors (Switzerland)*, vol. 14, no. 1. MDPI, pp. 144–169, Jan. 01, 2014. doi: 10.3390/s140100144.

[50] R. Mukherjee, J. Basu, P. Mandal, and P. K. Guha, “A review of micromachined thermal accelerometers,” *Journal of Micromechanics and Microengineering*, vol. 27, no. 12. Institute of Physics Publishing, Nov. 16, 2017. doi: 10.1088/1361-6439/aa964d.

[51] James Fennally, “Capacitive Vs Thermal MEMS for High-Vibration Applications,” 2016. doi: https://www.automation.com/en-us/articles/2016-1/capacitive-vs-thermal-mems-for-high-vibration-appl.

[52] L. Lin and J. Jones, “A liquid-filled buoyancy-driven convective micromachined accelerometer,” *Journal of Microelectromechanical Systems*, vol. 14, no. 5, pp. 1061–1069, Oct. 2005, doi: 10.1109/JMEMS.2005.856651.

[53] T. See-Ho, M. Abdul Haseeb, K. Karim S., P. Ash, and L. Albert M., “Monolithically fabricated polymermems 3-axis thermal accelerometers designed for automated wirebonder assembly,” in *2008 IEEE 21st International Conference on Micro Electro Mechanical Systems*, Tucson, AZ, USA, 2008, pp. 880–883.

[54] A. H. Ma and A. M. Leung, “Three-axis thermal accelerometer based on buckled cantilever microstructure,” in *IEEE Sensors Conference*, Lecce, Italy, 2008, pp. 1492–1495.

[55] R. Mukherjee, P. Mandal, and P. K. Guha, “Sensitivity improvement of a dual axis thermal accelerometer with modified cavity structure,” *Microsystem Technologies*, vol. 23, no. 12, pp. 5357–5363, Dec. 2017, doi: 10.1007/s00542-017-3338-4.

[56] L. Jiang, Y. Cai, H. Liu, and Y. Zhao, “A micromachined monolithic 3 axis accelerometer based on convection heat transfer,” in *The 8th Annual IEEE International Conference on Nano/Micro Engineered and Molecular Systems*, Suzhou, China, 2013, pp. 248–251.

[57] X. Wang, W. Xu, Izhar, and Y. K. Lee, “Theoretical and Experimental Study and Compensation for Temperature Drifts of Micro Thermal Convective Accelerometer,” *Journal of Microelectromechanical Systems*, vol. 29, no. 3, pp. 277–284, Jun. 2020, doi: 10.1109/JMEMS.2020.2977950.

[58] H. Farahani, J. K. Mills, and W. L. Cleghorn, “Design, fabrication and analysis of micromachined high sensitivity and 0% cross-axis sensitivity capacitive accelerometers,” *Microsystem Technologies*, vol. 15, no. 12, pp. 1815–1826, Dec. 2009, doi: 10.1007/s00542-009-0895-1.

[59] Z. Ghemari and S. Saad, “Reducing the measurement error to optimize the sensitivity of the vibration sensor,” *IEEE Sens J*, vol. 14, no. 5, pp. 1527–1532, 2014, doi: 10.1109/JSEN.2014.2298493.

[60] Y. W. Hsu, J. Y. Chen, H. T. Chien, S. Chen, S. T. Lin, and L. P. Liao, “New capacitive low-g triaxial accelerometer with low cross-axis sensitivity,” *Journal of Micromechanics and Microengineering*, vol. 20, no. 5, 2010, doi: 10.1088/0960-1317/20/5/055019.

[61] J. H. K. and K. N. Chae, “A CMOS-compatible high aspect ratio silicon-on-glass in-plane micro-accelerometer,” *Journal of Micromechanics and Microengineering*, vol. 15, no. 2, p. 336, 2004.

[62] A. Ravi Sankar, S. Das, and S. K. Lahiri, “Cross-axis sensitivity reduction of a silicon MEMS piezoresistive accelerometer,” *Microsystem Technologies*, vol. 15, no. 4, pp. 511–518, Apr. 2009, doi: 10.1007/s00542-008-0740-y.

[63] S. Gao, Z. Zhou, X. Bi, and L. Feng, “A Low Cross-Axis Sensitivity Micro-Grating Accelerometer with Double-Layer Cantilever Beams,” *IEEE Sens J*, vol. 21, no. 15, pp. 16503–16509, Aug. 2021, doi: 10.1109/JSEN.2021.3077303.

[64] H. Ghasemzadeh Momen, H. Tavakoli, and E. Abbaspour Sani, “A 3-axis MEMS capacitive accelerometer free of cross axis sensitivity,” in *24th Iranian Conference on Electrical Engineering (ICEE)*, 2016, pp. 1491–1494.

[65] A. M. Leung, J. Jones, E. Czyzewska, J. Chen, and M. Pascal, “Micromachined accelerometer with no proof mass.”

[66] D. Goustouridis, G. Kaltsas, and A. G. Nassiopoulou, “A silicon thermal accelerometer without solid proof mass using porous silicon thermal isolation,” *IEEE Sens J*, vol. 7, no. 7, pp. 983–988, Jul. 2007, doi: 10.1109/JSEN.2007.896559.

[67] B. Mezghani, F. Tounsi, and M. Masmoudi, “Development of an accurate heat conduction model for micromachined convective accelerometers,” *Microsystem Technologies*, vol. 21, no. 2, pp. 345–353, Feb. 2015, doi: 10.1007/s00542-014-2079-x.

[68] M. Han *et al.*, “Sensitivity and frequency-response improvement of a thermal convection-based accelerometer,” *Sensors (Switzerland)*, vol. 17, no. 8, Aug. 2017, doi: 10.3390/s17081765.

[69] J. Courteaud, P. Combette, N. Crespy, G. Cathebras, and A. Giani, “Thermal simulation and experimental results of a micromachined thermal inclinometer,” *Sens Actuators A Phys*, vol. 141, no. 2, pp. 307–313, Feb. 2008, doi: 10.1016/j.sna.2007.09.008.

[70] J. Jones, E. Czyzewska, J. Chen, and B. Woods, “MICROMACHINED ACCELEROMETER BASED ON CONVECTION HEAT TRANSFER.”

[71] R.K. Singal, *Refrigeration and Psychrometric Charts With Property Tables (S.I. Units)*. Delhi, India: S.K. Kataria & Sons, 2006.

[72] Steve Nevey, “Fluent Realize Your Product Promise ™.”

[73] KEVIN Y. MA, PAKPONG CHIRARATTANANON, SAWYER B. FULLER, and ROBERT J. WOOD, “Controlled flight of a biologically inspired, insect-scale robot,” *Science (1979)*, vol. 340, no. 6132, pp. 603–607, 2013, doi: 10.1126/science.1232758.

[74] R. J. Wood *et al.*, “Progress on ‘pico’ air vehicles,” in *International Journal of Robotics Research*, Sep. 2012, pp. 1292–1302. doi: 10.1177/0278364912455073.

[75] M. Lee, G. Park, C. Park, and C. Kim, “Improvement of Grid Independence Test for Computational Fluid Dynamics Model of Building Based on Grid Resolution,” *Advances in Civil Engineering*, vol. 2020, 2020, doi: 10.1155/2020/8827936.

[76] ML Engineering Content Editor, “Looking To Element Quality In ANSYS® Meshing(Illustrated Expression).”

[77] ML Engineering Content Editor, “Aspect Ratio Mesh Metric In ANSYS® Meshing(Illustrated Expression).”

[78] O. Yoshifumi, “Fast algorithms for particle searching and positioning by cell registration and area comparison,” *Trends in Computer Science and Information Technology*, pp. 007–016, Mar. 2021, doi: 10.17352/tcsit.000032.

[79] H. B. Nguyen, F. Mailly, L. Latorre, and P. Nouet, “A new monolithic 3-axis thermal convective accelerometer: principle, design, fabrication and characterization,” *Microsystem Technologies*, vol. 21, no. 9, pp. 1867–1877, Sep. 2015, doi: 10.1007/s00542-014-2254-0.

[80] A. Garraud, P. Combette, F. Pichot, J. Courteaud, B. Charlot, and A. Giani, “Frequency response analysis of an accelerometer based on thermal convection,” *Journal of Micromechanics and Microengineering*, vol. 21, no. 3, Mar. 2011, doi: 10.1088/0960-1317/21/3/035017.

Appendix A: Locating Cell IDs User-defined Functions (UDFs) code

Cell ID for temperature sensors.c.c

```
#include "udf.h"

real Volumne = 0.0;

DEFINE_SOURCE(energy, c, t, dS, eqn)
{
real x[ND_ND];
real source;

real xmin_i1, xmax_i1, ymin_i1, ymax_i1, zmin_i1, zmax_i1;
real xmin_i2, xmax_i2, ymin_i2, ymax_i2;
real xmin_i3, xmax_i3, ymin_i3, ymax_i3;
real xmin_i4, xmax_i4, ymin_i4, ymax_i4;

C_CENTROID(x, c, t);

xmin_i1= 0.0004;
xmax_i1= 0.0006;

xmin_i2=-0.0042;
xmax_i2=-0.0038;

ymin_i3=-0.0006;
ymax_i3=-0.0004;

ymin_i4=-0.0042;
ymax_i4=-0.0038;

zmin_i1= 0.0039;
zmax_i1= 0.0041;

ymin_i2= 0.0004;
ymax_i2= 0.0006;

xmin_i4=-0.0006;
xmax_i4=-0.0004;

if(x[0]>xmin_i1 && x[0]<xmax_i1 && x[1]>ymin_i2 && x[1]<ymax_i2 && x[2]>zmin_i1 && x[2]<zmax_i1 ||
 x[0]>xmin_i2 && x[0]<xmax_i2 && x[1]>ymin_i2 && x[1]<ymax_i2 && x[2]>zmin_i1 && x[2]<zmax_i1 ||
 x[0]>xmin_i4 && x[0]<xmax_i4 && x[1]>ymin_i3 && x[1]<ymax_i3 && x[2]>zmin_i1 && x[2]<zmax_i1 ||
 x[0]>xmin_i4 && x[0]<xmax_i4 && x[1]>ymin_i4 && x[1]<ymax_i4 && x[2]>zmin_i1 && x[2]<zmax_i1)
{
    source = 0.1/C_VOLUME(c,t);
    dS[eqn] = 0.0;

    printf("here %d %f %f %f\n ", c, x[0], x[1], x[2]);
}
else
```

Appendix B: Defining Source and Motion UDF code

SOURCE.c

```
#include "udf.h"

real Volume=0.0;

DEFINE_SOURCE(energy, c, t, dS, eqn)
{
real x[ND_ND];
real source;

int i1=49962,i2=119862,i3=84912,i4=154812;
/* i1=左 i2=下 i3=上 i4=右 */ /* i1=left i2=lower i3=upper i4=right */


    if(c==i1 || c==i2 || c==i3 || c==i4)
{
source = 0.04/C_VOLUME(c,t);
dS[eqn] = 0.0;
}
else
{
source = 0.0;
dS[eqn] = 0.0;
}
return source;
}

DEFINE_EXECUTE_AT_END(execute_at_end_X11)
{
    real temp13 = 0;
    real p13 = 0;
    Domain *d = Get_Domain(1);
    Thread *t;
    cell_t c;

    thread_loop_c(t,d)
    {
        begin_c_loop(c,t)
        {
        if (c==81612)
        {
            temp13 = C_T(c,t);
            p13 = C_P(c,t);
        }
        }
        end_c_loop(c,t)
    }
Message("%f %f \n", CURRENT_TIME, temp13);
```

```
FILE *ri = fopen("T_X11.data","a");
fprintf(ri, "%f %f\n", CURRENT_TIME, temp13);
if (ri) fclose(ri);

FILE *riq = fopen("P_X11.data","a");
fprintf(riq, "%f %f\n", CURRENT_TIME, p13);
if (riq) fclose(riq);
}

DEFINE_EXECUTE_AT_END(execute_at_end_X12)
{
    real temp1370 = 0;
    real p1370 = 0;
    Domain *d = Get_Domain(1);
    Thread *t;
    cell_t c;

    thread_loop_c(t,d)
    {
        begin_c_loop(c,t)
        {
        if (c==88212)
        {
            temp1370 = C_T(c,t);
            p1370 = C_P(c,t);
        }
        }
        end_c_loop(c,t)
    }
Message("%f %f \n", CURRENT_TIME, temp1370);

FILE *ribs = fopen("T_X12.data","a");
fprintf(ribs, "%f %f\n", CURRENT_TIME, temp1370);
if (ribs) fclose(ribs);

FILE *riqbs = fopen("P_X12.data","a");
fprintf(riqbs, "%f %f\n", CURRENT_TIME, p1370);
if (riqbs) fclose(riqbs);
}
```

CGMOTION.c

```
#include "udf.h"

DEFINE_CG_MOTION(CGMotion, dt, vel, omega, time, dtime)
{
vel[0]=19.62*time;
vel[1]=0.0;
vel[2]=0.0;

omega[0]=0.0;
omega[1]=0.0;
omega[2]=8.72665;
}
```

Appendix C: MATLAB code for obtaining inverse functions

```
surf (x,y,tx);
hold off;
set(gca,'YDir','reverse');
xlabel('Acceleration (m/s^2)');
ylabel('Amplitude (m)');
zlabel('Maximum temperature difference (K)');
shading interp;
colormap jet;
hold off;
plot3(xx,yy,tx,'o','Color','b','MarkerSize',7,'MarkerFaceColor','b');
hold off;
surf (x,y,tz);
hold off;
set(gca,'YDir','reverse');
xlabel('Acceleration (m/s^2)');
ylabel('Amplitude (m)');
zlabel('Maximum temperature difference (K)');
shading interp;
colormap jet;
plot3(xx,yy,tz,'o','Color','b','MarkerSize',7,'MarkerFaceColor','#FF00
FF');
hold off;
xv = linspace (9.81,39.24,34);
yv = linspace (0.03,0.09,34);
[X,Y]=meshgrid(xv,yv);
TX = griddata (x,y,tx,X,Y);
TZ = griddata (x,y,tz,X,Y);
surf (X,Y,TX);
hold on;
surf (X,Y,TZ);
hold off;
surf (TX,TZ,X);
set (gca,'YDir','reverse','FontSize',14);
xlabel('?T X_m_a_x (K)');
ylabel('?T Z_m_a_x (K)');
zlabel('Acceleration (m/s^2)');
view(270,0);
```

Appendix D: MATLAB code for obtaining 2D mapping plots

```
plot ([505.5 505.5],[329 441],'k','LineWidth',0.1);
hold on;
plot ([516 516],[329 441],'k','LineWidth',0.1);
plot ([526.5 526.5],[329 441],'k','LineWidth',0.1);

plot ([495 537],[357 357],'k','LineWidth',0.1);
plot ([495 537],[385 385],'k','LineWidth',0.1);
plot ([495 537],[413 413],'k','LineWidth',0.1);

plot ([497.3 499.4],[425.9 381.3],'r','LineWidth',3);
plot ([499.4 495.6],[381.3 353.7],'r','LineWidth',3);
plot ([495.6 496.1],[353.7 337.6],'r','LineWidth',3);

plot ([507.0 519.3],[435.8 393.7],'r','LineWidth',3);
plot ([519.3 516.1],[393.7 355.9],'r','LineWidth',3);
plot ([516.1 512.2],[355.9 333.4],'r','LineWidth',3);

plot ([512.6 529.5],[440.6 404.0],'r','LineWidth',3);
plot ([529.5 527.1],[404.0 361.3],'r','LineWidth',3);
plot ([527.1 523.5],[361.3 332.3],'r','LineWidth',3);

plot ([514.3 536.2],[440.0 408.1],'r','LineWidth',3);
plot ([536.2 534.8],[408.1 361.0],'r','LineWidth',3);
plot ([534.8 533.2],[361.0 329.3],'r','LineWidth',3);

plot ([497.3 507.0],[425.9 435.8],'r','LineWidth',3);
plot ([507.0 512.6],[435.8 440.6],'r','LineWidth',3);
plot ([512.6 514.3],[440.6 440.0],'r','LineWidth',3);

plot ([499.4 519.3],[381.3 393.7],'r','LineWidth',3);
plot ([519.3 529.5],[393.7 404.0],'r','LineWidth',3);
plot ([529.5 536.2],[404.0 408.1],'r','LineWidth',3);

plot ([495.6 516.1],[353.7 355.9],'r','LineWidth',3);
plot ([516.1 527.1],[355.9 361.3],'r','LineWidth',3);
plot ([527.1 534.8],[361.3 361.0],'r','LineWidth',3);

plot ([496.1 512.2],[337.6 333.4],'r','LineWidth',3);
plot ([512.2 523.5],[333.4 332.3],'r','LineWidth',3);
plot ([523.5 533.2],[332.3 329.3],'r','LineWidth',3);
```

```
xlabel('T-Y12_m_a_x (K)');
ylabel('T-Y12_m_i_n (K)');
set(gca,'FontSize',14);

xlim([495 537])
ylim([329 441])

plot(507.2,404.1,'o','MarkerSize',12,'MarkerFaceColor','m','MarkerEdgeColor','k')
```